

Chandra X-Ray Spectroscopy of the Focused Wind in the Cygnus X-1 System

II. The Nondip Spectrum in the Low/Hard State – Modulations with Orbital Phase

Ivica Miškovíčová¹, Natalie Hell^{1,2}, Manfred Hanke¹, Michael A. Nowak³, Katja Pottschmidt^{4,5}, Norbert S. Schulz³, Victoria Grinberg^{1,3}, Refiz Duro^{1,6}, Oliwia K. Madej^{7,8}, Anne M. Lohfink⁹, Jérôme Rodriguez¹⁰, Marion Cadolle Bel¹¹, Arash Bodaghee¹², John A. Tomsick¹³, Julia C. Lee¹⁴, Gregory V. Brown², and Jörn Wilms¹

¹ Dr. Karl Remeis-Sternwarte and Erlangen Centre for Astroparticle Physics, Universität Erlangen-Nürnberg, Sternwartstr. 7, 96049 Bamberg, Germany*

² Lawrence Livermore National Laboratory, 7000 East Ave., Livermore, CA 94550, USA

³ MIT Kavli Institute for Astrophysics and Space Research, NE80, 77 Mass. Ave., Cambridge, MA 02139, USA

⁴ CRESST, University of Maryland Baltimore County, 1000 Hilltop Circle, Baltimore, MD 21250, USA

⁵ NASA Goddard Space Flight Center, Astrophysics Science Division, Code 661, Greenbelt, MD 20771, USA

⁶ AIT Austrian Institute of Technology GmbH, Donau-City-Str. 1, 1220 Vienna, Austria

⁷ Department of Astrophysics/IMAPP, Radboud University Nijmegen, P.O. Box 9010, 6500 GL Nijmegen, The Netherlands

⁸ SRON Netherlands Institute for Space Research, Sorbonnelaan 2, 3584 CA Utrecht, The Netherlands

⁹ Institute of Astronomy, University of Cambridge, Madingley Road, Cambridge CB3 0HA, United Kingdom

¹⁰ Laboratoire AIM, UMR 7158, CEA/DSM-CNRS-Université Paris Diderot, IRFU/SAP, 91191 Gif-sur-Yvette, France

¹¹ Max Planck Computing and Data Facility, Gießenbachstr. 2, 85748 Garching, Germany

¹² Department of Chemistry, Physics, and Astronomy, Georgia College & State University, Milledgeville, GA 31061

¹³ Space Sciences Laboratory, 7 Gauss Way, University of California, Berkeley, CA 94720-7450, USA

¹⁴ Harvard John A. Paulson School of Engineering and Applied Sciences, and Harvard-Smithsonian Center for Astrophysics, 60 Garden Street MS-6, Cambridge, MA 02138, USA

Received / Accepted

ABSTRACT

The accretion onto the black hole in the system HDE 226868/Cygnus X-1 is powered by the strong line driven stellar wind of the O-type donor star. We study the X-ray properties of the stellar wind in the hard state of Cyg X-1 as determined with data from the *Chandra* High Energy Transmission Gratings. Large density and temperature inhomogeneities are present in the wind, with a fraction of the wind consisting of clumps of matter with higher density and lower temperature embedded in a photoionized gas. Absorption dips observed in the light curve are believed to be caused by these clumps. This work concentrates on the non-dip spectra as a function of orbital phase. The spectra show lines of H-like and He-like ions of S, Si, Na, Mg, Al and highly ionized Fe (Fe xvii–Fe xxiv). We measure velocity shifts, column densities, and thermal broadening of the line series. The excellent quality of these five observations allows us to investigate the orbital phase dependence of these parameters. We show that the absorber is located close to the black hole. Doppler shifted lines point at a complex wind structure in this region, while emission lines seen in some observations are from a denser medium than the absorber. The observed line profiles are phase dependent. Their shapes vary from pure, symmetric absorption at the superior conjunction to P Cygni profiles at the inferior conjunction of the black hole.

Key words. accretion, accretion disks – stars: individual (HDE 226868, Cyg X-1) – stars: winds, outflows – X-rays: binaries

1. Introduction

In the fifty years of persistent X-ray activity since its discovery in 1964 (Bowyer et al. 1965), the High-Mass X-ray Binary Cygnus X-1 (Cyg X-1) has become one of the best known X-ray sources, but there are still many open questions even in regard to one of its most basic properties, the nature of the accretion process. The system consists of the supergiant O9.7 Iab type star HDE 226868 (Walborn 1973) and a compact object in a 5.6 d orbit (Webster & Murdin 1972; Brocksopp et al. 1999; Gies et al. 2003) with an inclination of $i = 27.1 \pm 0.8$ (Orosz et al. 2011). The system has a distance $d = 1.86^{+0.12}_{-0.11}$ kpc (Xiang et al. 2011; Reid et al. 2011). Based on these measurements, masses of $M_2 = 19.2 \pm 1.9 M_\odot$ for

the companion star and $M_1 = 14.8 \pm 1.0 M_\odot$ for the compact object have been deduced (Orosz et al. 2011).

With a mass loss rate of $\sim 10^{-6} M_\odot \text{ year}^{-1}$ (Herrero et al. 1995), HDE 226868 shows a strong wind. Such winds are driven by radiation pressure, due to copious absorption lines present in the ultraviolet part of the spectrum on material in the stellar atmosphere (line-driven or Castor, Abbott, & Klein, 1975, [CAK] wind model), can reach very high velocities ($v_\infty \gg 2000 \text{ km s}^{-1}$; Muijres et al. 2012), and are only produced by hot, early type O- or B-stars. Simulations show that a steady solution of line-driven winds is not possible, i.e., perturbations are present in the wind (Feldmeier et al. 1997), causing variations of density, velocity and temperature, which compress the gas into small, cold, and overdense structures, often referred to as “clumps” (Oskinova et al. 2012; Sundqvist & Owocki 2013, and references therein).

* joern.wilms@sternwarte.uni-erlangen.de

The existence of clumps is supported by observations of transient X-ray absorption dips (lower flux) in the soft X-ray light curves of such systems. Sako et al. (1999) estimate that more than 90% of the total wind mass in Vela X-1 is concentrated in clumps, while the ionized gas covers more than 95% of the wind volume. Clumpiness with a filling factor of 0.09–0.10 has been confirmed in Cyg X-1 by Rahoui et al. (2011).

Strong tidal interactions between the star and the black hole and centrifugal forces make the wind distorted and asymmetric. Both the wind density and the mass loss rate are enhanced close to the binary axis, creating a so-called “*focused wind*” (Friend & Castor 1982). Evidence for the presence of such a wind around HDE 226868, which fills more than $\sim 90\%$ of its Roche volume (Gies & Bolton 1986), is the strong modulation of the He II $\lambda 4686$ emission line with orbital phase (Gies & Bolton 1986) and the strong phase dependence of other optical absorption lines, which are deepest around orbital phase $\phi_{\text{orb}} = 0$ (Gies et al. 2003), i.e., during the superior conjunction of the black hole. Further evidence comes from the modelling of the IR continuum emission (Rahoui et al. 2011). Finally, in the X-rays, the overall absorption column density and dipping vary strongly with orbital phase and are largest at $\phi_{\text{orb}} \sim 0.0$ (e.g., Li & Clark 1974; Mason et al. 1974; Parsignault et al. 1976; Pravdo et al. 1980; Remillard & Canizares 1984; Kitamoto et al. 1984, 1989; Wen et al. 1999; Bałucińska-Church et al. 2000; Feng & Cui 2002; Lachowicz et al. 2006; Poutanen et al. 2008; Hanke et al. 2009), consistent with the focused wind picture (e.g., Li & Clark 1974; Remillard & Canizares 1984; Bałucińska-Church et al. 2000; Poutanen et al. 2008). Due to the presence of the focused wind, the accretion process in Cyg X-1 is not primarily wind accretion like in other HMXBs such as Vela X-1, SMC X-1, or 4U 1700–37 (Bondi & Hoyle 1944; Blondin & Woo 1995; Blondin 1994; Blondin et al. 1991), but a small accretion disk is present. Evidence for this disk comes from detections of the disk’s thermal spectrum (Bałucińska-Church et al. 1995; Priedhorsky et al. 1979), an X-ray disk reflection component, and a strong and broad Fe K α line (Tomsick et al. 2014; Duro et al. 2011, and references therein).

Black hole binaries show two characteristic behaviors, called the low/hard and the high/soft state. These states differ in the shape of the X-ray spectrum, the timing properties, and the radio emission (Fender et al. 1999; Belloni 2004; Wilms et al. 2006; Belloni 2010, and references therein). The spectrum of Cyg X-1 in the hard state is well described by a hard, exponentially cut-off broken powerlaw with photon index $\Gamma \sim 1.7$ (Wilms et al. 2006). During the soft state, the power law is steeper ($\Gamma \sim 2.5$) and a luminous and less variable thermal disk component appears (Wilms et al. 2006).

Cyg X-1 is often considered to be a hard state source, as it spent most of the time in the hard state (Grinberg et al. 2013). Transitions into the soft state are observed every few years and “failed state transitions”, where the soft state is not entirely reached, are also possible (Pottschmidt et al. 2003). Since 2010 the source’s behavior has been rather unusual and it has spent significantly more time in the soft state. See Grinberg et al. (2013) for a discussion of the long-term changes in Cyg X-1 from 1996 until the end of 2012.

Since X-rays from the black hole propagate through the stellar wind, we can use these X-rays to probe its structure. For such a study it is essential that the source is in the hard state or the hard-intermediate state. The strong X-ray emission during the soft state is sufficient to completely photoionize the stellar wind. As a consequence, the wind is suppressed because the radiative

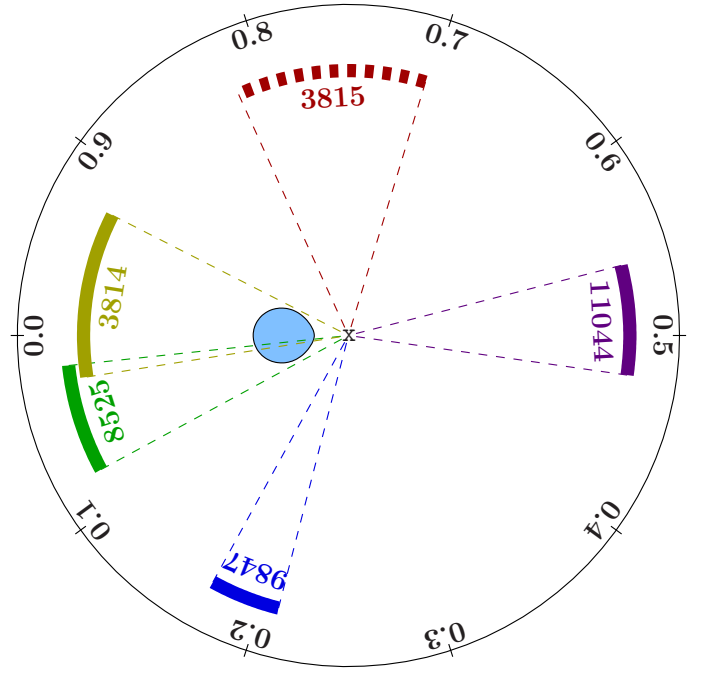


Fig. 1. Orbital phase coverage of the *Chandra* observations of Cyg X-1 in the hard state analyzed in this work. Full arcs (dashed arcs) display TE mode (CC mode; for explanation see Sect. 2.3) observations. The labels correspond to the *Chandra* ObsIDs. Phase $\phi_{\text{orb}} = 0$ corresponds to the superior conjunction of the black hole.

driving force of the UV photons from the donor star is reduced as the ionized gas is transparent for UV radiation.

In this paper, we extend earlier work on *Chandra* high-resolution grating spectra from Cygnus X-1 studying the ionized material of the stellar wind of HDE 226868 during the low/hard state (Hanke et al. 2009, hereafter paper I). We perform a detailed study of four observations at phases $\phi_{\text{orb}} \sim 0.05$, ~ 0.2 , ~ 0.5 , and ~ 0.75 , and combine it with previous results of the observation at ~ 0.95 (paper I). These data provide a unique set of observations that allows us to probe all prominent parts of the wind of Cyg X-1 (Fig. 1). Our aim is to describe the complex structure and the dynamics of the stellar wind. Sect. 2 summarizes observations and data used in the analysis. In Sect. 3 and Sect. 4, we present the data analysis and results related to the continuum fitting and the H-like and He-like absorption lines observed in the non-dip spectra. In Sect. 5, we discuss their modulation with orbital phase. Sect. 6 discusses line profile variations and results from plasma density diagnostics. We summarize our conclusions in Sect. 7. Overview tables and plots of all full range spectra are given in appendix A. Technical issues related to the analysis are discussed in appendices B and C.

2. Observations and data reduction

2.1. Selection of Observations

The main purpose of this paper is to study the variation of the X-ray spectrum with orbital phase during the hard state. Only six of the 17 available *Chandra*-HETG observations meet this condition: ObsIDs 2415, 3814, 3815, 8525, 9847, and 11044 (see Sect. 2.2 for a discussion of the state classification). All other *Chandra* observations of Cyg X-1 either caught the source in the high/soft state or were too short to obtain spectra of a sufficient

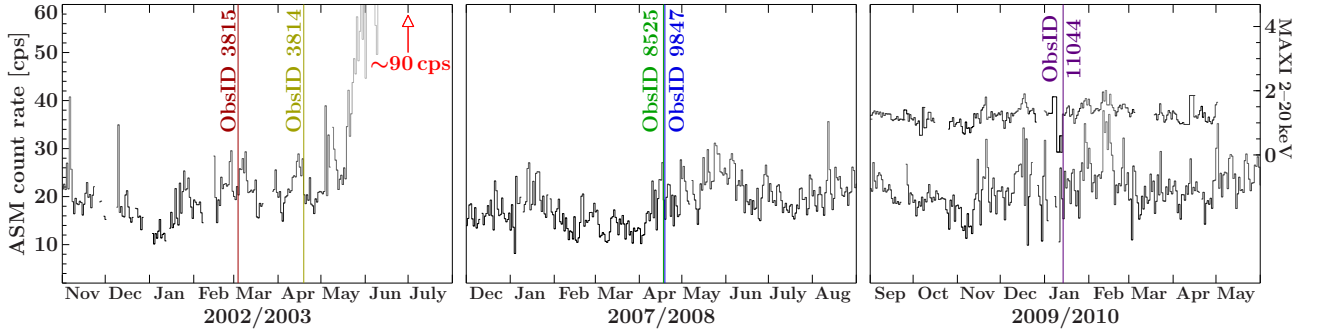


Fig. 2. 1.5–12 keV *RXTE*-All-Sky Monitor count rate of Cyg X-1 with one day binning in the intervals of nine months during 2003, 2008 and 2010 centered at the times of *Chandra* observations: ObsIDs 3815 and 3814 (left), 8525 and 9847 (middle), and 11044 (right), marked by vertical lines. The right panel also shows the MAXI light curve.

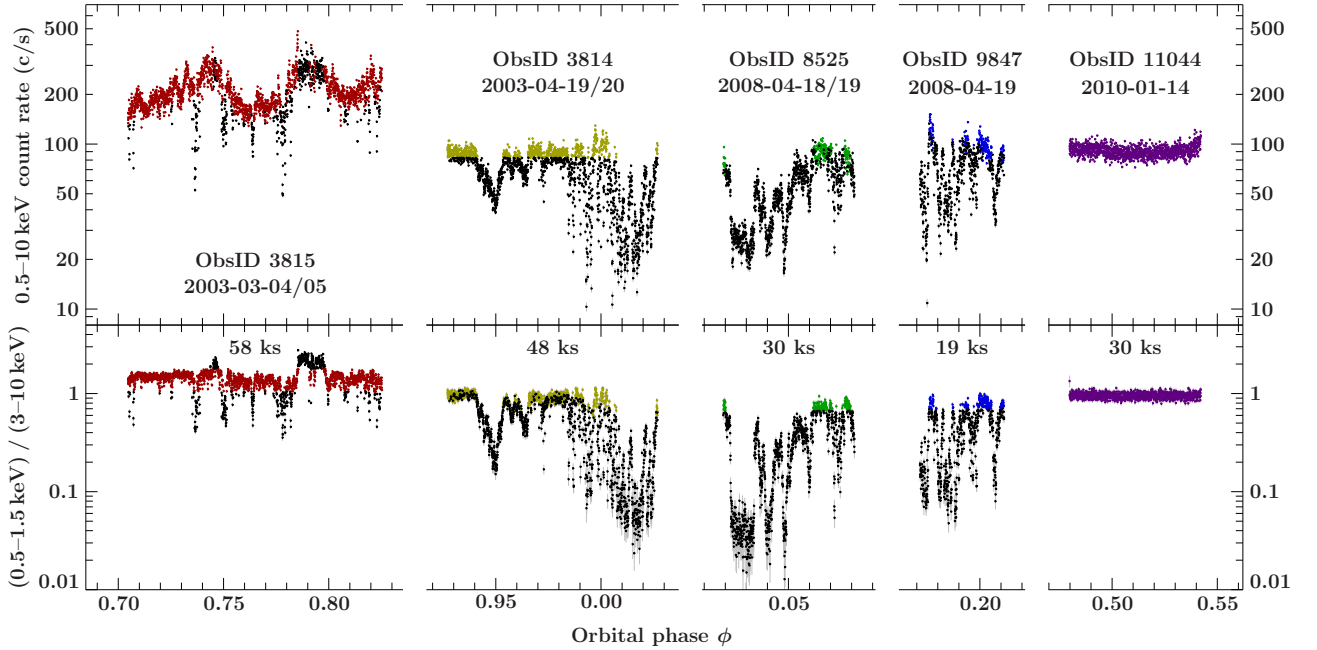


Fig. 3. *Upper panel:* Lightcurves of all five observations as a function of orbital phase. *Lower panel:* variation of the hardness ratio. Except for the somewhat softer hard-intermediate state observation ObsID 3815, all observations were in the low/hard state. Dips are strongest at $\phi_{\text{orb}} \sim 0.0$, still present at $\phi_{\text{orb}} \sim 0.2$ and $\phi_{\text{orb}} \sim 0.75$, and they vanish at $\phi_{\text{orb}} \sim 0.5$. Colors indicate the parts of the observations used in the analysis (see Fig. 1), while data in black were excluded from the analysis.

signal-to-noise ratio. ObsID 2415, taken during the intermediate state at $\phi_{\text{orb}} \sim 0.76$ was already analyzed by Miller et al. (2005). Table 1 gives a log of the remaining observations studied in this paper and Fig. 1 depicts their orbital coverage. Results on ObsID 3814 from paper I will be combined with these new results in Sect. 4 and 5.

To gauge the quality of the continuum modeling, we use simultaneous pointed *RXTE* observations (Sect. 3.2), which were reduced using our standard procedures as described, e.g., by Wilms et al. (2006) or Grinberg et al. (2015).

2.2. Source State

Figure 2 shows the *RXTE* All-Sky-Monitor (ASM; Levine et al. 1996) lightcurve of Cyg X-1 around the times of the *Chandra* observations. The average daily ASM data point towards similar conditions during the first four observations. According to the scheme of Grinberg et al. (2013), all four observations are found

in the hard state, with low countrate (14–18 cps) in ObsIDs 3814, 8525 and 9847 and a higher countrate of 26 cps in ObsID 3815.

ObsID 11044 was taken during the time when ASM was deteriorating (Vrtilek & Boroson 2013; Grinberg et al. 2013). We therefore used MAXI data (Matsuoka et al. 2009) for the assessment of this observation. Six MAXI measurements are simultaneous with ObsID 11044: they all show the source in the hard state as defined by Grinberg et al. (2013).

2.3. Data Reduction

For the spectral analysis we used the first order spectra of *Chandra*'s high and medium energy gratings (HEG, MEG; Canizares et al. 2005). Most HETG observations of Cyg X-1 in the analysis were performed in timed exposure (TE) mode of the Advanced CCD imaging spectrometer (ACIS; Garmire et al. 2003). In this mode data are nominally accumulated for a 3.2 s frame time before being transferred into a framestore and read out, increasing the probability of pile up. In the cases of

Table 1. Log of hard-state *Chandra*-HETGS observations of Cyg X-1 used in this paper.

ObsID	Start date		Mode	T_{exp} [ks]	ϕ_{orb}	Count rates		h	Non-dip spectrum	
	Date yy-mm-dd	MJD				r_{ASM} [cps]	r_{Chandra} [cps]		$T_{\text{exp,non-dip}}$ [ks]	$L_{0.5-10 \text{ keV}}$ [10^{37} erg/s]
3815	03-03-04	52702	CC/g	58.4	0.70–0.82	25.8	210.5	1.05–1.8	45	0.67
3814	03-04-19	52748	TE/g	48.3	0.93–0.03	17.5	88.6	–	16.1	0.39 ^a
8525	08-04-18	54574	TE/g	30.1	0.02–0.08	14.2	87.5	0.667–0.94	4.4	0.43
9847	08-04-19	54575	TE/g	19.3	0.17–0.21	18.0	100.9	0.692–1.0	4.4	0.49
11044	10-01-14	55210	TE/g	30.1	0.48–0.54	18.4	91.1	–	30.1	0.41

Notes. Mode: CC/g – Continuous Clocking, graded; TE/g – Timed Exposure, graded; T_{exp} : exposure time; ϕ_{orb} : orbital phase according to the ephemeris of Gies et al. (2003); r_{ASM} : *RXTE*-ASM (1.5–12 keV) count rate, averaged over the observation; r_{Chandra} : *Chandra* spectral (non-dip) count rate; h is the hardness ratio of the *Chandra* first order count rates in the 0.5–1.5 keV band to those in the 3–10 keV band; $T_{\text{exp,non-dip}}$ – exposure time after exclusion of dips. Note that ObsID 8525 and 9847 were scheduled as part of a multi-satellite campaign onto the system. For technical reasons this 50 ksec observation was split into two parts. $L_{0.5-10 \text{ keV}}$ – source luminosity in the 0.5–10 keV energy range, derived from the non-dip spectra assuming a source distance of 1.86 kpc (Xiang et al. 2011; Reid et al. 2011). ^a Hanke et al. (2009), corrected for the newer source distance.

ObsIDs 3814, 8525, 9847, and 11044, the frame time was reduced to 1.7 s by using a 512 row CCD subarray readout.

In even brighter cases, as in ObsID 3815, where Cyg X-1 was in the hard-intermediate state, a continuous clocking (CC) mode was applied to avoid pile up and conserve line features. Here the CCD rows are read out continuously, which reduces the exposure per row to 2.85 ms (Garmire et al. 2003) and no effects from pile up are expected. The application of CC-mode comes at the expense of one spatial dimension as the image is then reduced to 1024×1 pixel frames and the y-image dimension is lost. As a consequence, all image photons including non-source dispersed photons such as from the source scattering halo get collapsed into the spectrum, order sorting becomes more difficult, and calibration uncertainties are higher leading to lesser determined continua. Some of these technical issues are discussed in detail in appendix B.

The data were processed with the standard *Chandra* Interactive Analysis of Observations (CIAO) software, version 4.2. Further analysis was done with the Interactive Spectral Interpretation System (ISIS), versions 1.6.1 and 1.6.2 (Houck & Denicola 2000). Cross-sections were taken from Verner et al. (1996), abundances from Wilms et al. (2000), and atomic data from the Atomic Database, AtomDB v. 2.0.1 (Foster et al. 2012). Due to the very low *Chandra* background (compared to the source), no background was subtracted from the final spectra. Data were grouped to a minimum signal-to-noise ratio of $S/N = 10$. Unless noted otherwise, all uncertainties are at the 90% level for one parameter of interest ($\Delta\chi^2 = 2.71$; Lampton et al. 1976).

For spectra from observations performed in TE mode the effect of pile-up has to be considered. In the first order spectra it causes a pure reduction of count rate. It is stronger in the MEG spectra than in the HEG spectra due to the lower dispersion and higher effective area of the MEG. The apparent flux reduction is most significant near 2 keV (6–7 Å) where the spectrometer has the largest efficiency and the highest count rates are obtained. As described in greater detail in paper I, pile up in the gratings can be modelled in ISIS using the nonlinear convolution model `simple_gpile2`. This model describes the reduction of the predicted source count rate, $S(\lambda)$, by pile up as

$$S'(\lambda) = S(\lambda) \cdot \exp(-\beta \cdot S_{\text{tot}}(\lambda)) \quad (1)$$

where the total count rate $S_{\text{tot}}(\lambda)$ is estimated from the effective area and the assumed (model) photon flux, and where the scale parameter β is a fit parameter. $S_{\text{tot}}(\lambda)$ includes the contributions

of the 1st, 2nd, and 3rd order spectra at the detector location corresponding to λ .

3. Continuum Modeling

3.1. Overview

A detailed look at the light curves and spectra of the five hard state observations allows us to probe the structure of the wind and its modulation with orbital phase. As shown in Fig. 3, dipping is clearly present for most of the orbit, but the dip frequency seems to be phase dependent. Light curves around $\phi_{\text{orb}} \sim 0.0$ are modulated by strong and complex absorption dips. Dipping occurs already at $\phi_{\text{orb}} \sim 0.7$ and has not ceased at $\phi_{\text{orb}} \sim 0.2$. The dip events become shorter and shallower as the black hole moves away from superior conjunction, as expected given that the line of sight through the densest regions of the (focused) stellar wind is longest for $\phi_{\text{orb}} \sim 0.0$. The data at $\phi_{\text{orb}} \sim 0.5$, which probe only the outer regions of the stellar wind, do not show any dipping. This distribution of dipping is consistent with theoretical predictions and observations that see the high-density focused wind close to the binary axis at $\phi_{\text{orb}} = 0$. A consequence is a high probability to see dipping events at $\phi_{\text{orb}} = 0$ and a much smaller probability for dipping at $\phi_{\text{orb}} = 0.5$ (Bałucińska-Church et al. 2000; Poutanen et al. 2008; Boroson & Vrtilek 2010).

The main goal of this paper is to study the effects of the stellar wind on the X-ray spectrum. The time intervals where the data are distorted by dips need to be removed from the analysis. Properties, dynamics, and origin of the dips will be discussed by Hell et al. (2013, 2014, in prep.). Following the discussion of Hanke et al. (2008), different stages of dipping can be defined based on different count rate levels in the light curve, or on its dependence in the color-color diagram, or on the softness ratio. According to Kitamoto et al. (1984) and confirmed by the lightcurves of our observations, dips can last from several seconds to more than 10 minutes, especially around superior conjunction. We therefore extracted light curves with a 25.5 s resolution, except for ObsID 3814 where 12.25 s were used (paper I), in order to be able to also identify short dipping intervals. For ObsIDs 3815, 8525, and 9847 the selection of non-dip intervals was based on the hardness ratio defined as (0.5–1.5 keV)/(3–10 keV). See Table 1 for the exact selection criteria, which vary between observations due to differences in the continuum shape, and the resulting non-dip exposure times. As shown in Fig. 3, the selection criteria work well for all observations, with only a small contribution due to residual dips with

low N_{H} remaining in the lightcurves. Choosing slightly different selection criteria shows that these residual dips do not affect our analysis. For ObsID 3814, the count-rate based selection of paper I is used. Since no dips are present in ObsID 11044, the full ~ 30 ks of exposure can be used in the analysis.

Residual dipping present in the “non-dip” spectra can influence our fitting results. In order to gauge the influence of dips on these spectra we relaxed the hardness criterion and also extracted a spectrum of ObsID 8525 which includes moderate dipping and refitted the continuum. The contaminated spectrum was chosen very conservatively, it corresponds to a hardness ≥ 0.449 in the lower panel of Fig. 3. In the combined spectrum, N_{H} changed by 15% from $5.5 \times 10^{21} \text{ cm}^{-2}$ to $6.3 \times 10^{21} \text{ cm}^{-2}$. Because of our much more conservative selection criteria, the systematic error in our non-dip spectra is significantly smaller than that. We estimate it to be of the same order of magnitude as the statistical errors of the fits.

3.2. Continuum Model

The extracted non-dip spectra are characterized by an absorbed continuum onto which a large number of absorption lines are superimposed. As we are not focusing on a physical interpretation of the continuum, we describe it with a simple empirical model that is flexible enough to give an accurate representation of the proper continuum spectrum, i.e., an absorbed power-law. Cross-checks with simultaneous broad-band spectra from *RXTE* performed during our *Chandra* observations show that our continuum parameters are in reasonable agreement between the two satellites. We look at two extreme observations, ObsID 3815 and 11044. In ObsID 11044 the *Chandra* spectrum is neither distorted by calibration features, nor influenced by strong absorption lines. Fitting the *Chandra* continuum model given in Table 2 to the simultaneous 3–6 keV PCA spectrum, leaving the normalization value free to vary to take into account the well-known flux-cross calibration issues between the PCA and other satellites (Nowak et al. 2011), gives a reasonable $\chi^2_{\text{red}} = 1.65$ ($\chi^2/\text{dof} = 9.95/6$) with consistent photon indices for the two instruments. While formally not a very good fit, the ratio between the data and the model in the PCA shows deviations of $<1\%$ and is therefore consistent with the calibration uncertainty of the PCA in this energy band (Jahoda et al. 2006; Shaposhnikov et al. 2012). The large χ^2 is therefore due to PCA calibration systematics. Note that the energy band chosen, 3–6 keV, represents the maximum overlap between the PCA and the HETGS, we deliberately do not extend the PCA data to higher energies because we are only interested in determining how well the continuum is described by the model in the HETGS band.

As a second example we consider the continuum of *Chandra* ObsID 3815, which had to be modeled using a complicated and nonphysical continuum. A direct comparison of this model with the contemporaneous *RXTE*-PCA data is complicated by the fact that these data were unfortunately taken during one of the deep dips in the lightcurve. We therefore extracted a *Chandra* spectrum from the aforementioned dip and made a comparison between strictly simultaneous data only. We modeled it with the same continuum model that was also used for the non-dip continuum, giving $A_{\text{PL}} = 1.38 \pm 0.04$, $\Gamma = 1.40 \pm 0.03$, $N_{\text{H}} = 0.33 \pm 0.01 \times 10^{22} \text{ cm}^{-2}$ and a $\chi^2_{\text{red}} = 1.07$ ($\chi^2/\text{dof} = 10550/9855$). Applying the same fit to the PCA, leaving N_{H} fixed at the *Chandra* value, leaving only the normalization a parameter, gives $A_{\text{PL}} = 1.61 \pm 0.01$ and the $\chi^2_{\text{red}} = 2.34$ ($\chi^2/\text{dof} = 14.07/6$). The ratio between the data and the model shows again

Table 2. Continuum parameters of ObsID 8525, 9847 and 11044

Parameter	ObsID 8525 $\phi_{\text{orb}} \sim 0.05$	ObsID 9847 $\phi_{\text{orb}} \sim 0.2$	ObsID 11044 $\phi_{\text{orb}} \sim 0.5$
power-law			
$A_{\text{PL}} [\text{s}^{-1} \text{ cm}^{-2} \text{ keV}^{-1}]$	$1.23^{+0.03}_{-0.02}$	1.45 ± 0.02	1.38 ± 0.01
Γ	$1.43^{+0.02}_{-0.01}$	1.45 ± 0.01	1.59 ± 0.01
TBnew			
$N_{\text{H}} [10^{22} \text{ cm}^{-2}]$	$0.55^{+0.03}_{-0.02}$	0.47 ± 0.02	0.56 ± 0.01
$N_{\text{Ne}} [10^{18} \text{ cm}^{-2}]$	0.77 ± 0.18	$1.13^{+0.14}_{-0.15}$	0.58 ± 0.05
$N_{\text{Fe}} [10^{17} \text{ cm}^{-2}]$	–	–	1.5 ± 0.2
simple_gpile2			
$\beta_{\text{HEG-1}}$	$4.40^{+0.26}_{-0.41}$	$3.8^{+0.1}_{-0.2}$	3.8 ± 0.1
$\beta_{\text{HEG+1}}$	$4.74^{+0.26}_{-0.40}$	4.01 ± 0.16	4.08 ± 0.08
$\beta_{\text{MEG-1}}$	$6.01^{+0.15}_{-0.20}$	5.69 ± 0.09	5.46 ± 0.04
$\beta_{\text{MEG+1}}$	$6.41^{+0.13}_{-0.17}$	6.41 ± 0.07	6.15 ± 0.03
χ^2	3174.49	3661.78	12142.47
dof	2985	3382	11040
χ^2_{red}	1.06	1.08	1.10

Notes. A_{PL} – flux density of the power-law at 1 keV; Γ – photon index of the power-law; N_{H} – hydrogen column density, N_{Ne} and N_{Fe} – neutral column densities of Ne and Fe; **simple_gpile2** β – pile-up scale parameters in units of $10^{-2} \text{ s } \text{\AA}$.

deviations of $\leq 1\%$, however, the residuals suggest that adjustment of the slope of power law would improve the fit. A fit with Γ left free, $A_{\text{PL}} = 1.72 \pm 0.06$, $\Gamma = 1.45 \pm 0.02$, is consistent with the original fit to within the error bars. The data-to-model ratio deviations lie below 0.5%. This best-fit has an unphysically good $\chi^2_{\text{red}} = 0.21$ ($\chi^2/\text{dof} = 1.04/5$), indicating that the systematic error in the PCA has been overestimated. Fitting the PCA data without applying a systematic error gives $\chi^2_{\text{red}} = 0.87$ ($\chi^2/\text{dof} = 4.34/5$). See Nowak et al. (2011), Wilms et al. (2006), and Gierliński et al. (1999) for physical continuum descriptions.

Neutral absorption is modelled with the TBnew model (Juett et al. 2006, paper I, and <http://pulsar.sternwarte.uni-erlangen.de/~wilms/research/tbnew>). Compared to the absorption model of Wilms et al. (2000), TBnew contains a better description of the absorption edges and allows a simple fitting of columns of individual elements (see, e.g., Hanke et al. 2010). In gratings data such an approach is possible when a strong absorption edge is present in the spectrum. For the wavelength range studied here, the most important edge is the Ne K-edge. Where indicated below, we therefore fitted the column of neutral Ne independently of N_{H} . Although K-edges of S, Si, Mg, and Na are also present, they are not as clearly visible in the spectra and the abundances of these elements were fixed to their interstellar values (Wilms et al. 2000). Taking into account pile up, the adopted continuum shape was

$$N_{\text{ph}}(E) = \text{simple_gpil2} \otimes (\text{TBnew} \times \text{powerlaw}). \quad (2)$$

In the following, we briefly discuss the continuum properties for the four observations modeled here. We refer to paper I for continuum description of the non-dip spectrum of ObsID 3814.

3.3. The Continuum of ObsIDs 8525 and 9847 ($\phi_{\text{orb}} \sim 0.05$ and $\phi_{\text{orb}} \sim 0.2$)

After filtering for dips only ~ 4.4 ks of non-dip data remain for each of the two observations. In order to stay above a signal-to-noise ratio of 10, the continua of these two observations were modeled in the wavelength range $2 \text{ \AA} - 15 \text{ \AA}$ for MEG and $2 \text{ \AA} - 12 \text{ \AA}$ for HEG. Best-fit parameters are listed in Table 2.

Both observations show many short, but strong, dips in the light curve. It is probable that even after the exclusion of dips, the non-dip spectrum is contaminated by faint dips, which may have an influence on parameters obtained in the analysis.

3.4. The Continuum of ObsID 11044 ($\phi_{\text{orb}} \sim 0.5$)

The high signal to noise ratio of this ~ 30 ks observation allows us to model the continuum in the range of $1.7 \text{ \AA} - 20 \text{ \AA}$. The continuum is well described by Eq. (2). The Ne- and also Fe-column densities were allowed to vary and are mainly constrained by the Ne K and Fe L_2 / L_3 edges at 14.3 \AA and $17.2 \text{ \AA} / 17.5 \text{ \AA}$, respectively, which are very prominent in the spectrum. Best fit parameters are again shown in Table 2. As also indicated by similar behavior in *RXTE*-ASM (Fig. 2), ObsID 11044 was performed in a similar state as ObsID 8525 ($\phi_{\text{orb}} \sim 0.05$) and 9847 ($\phi_{\text{orb}} \sim 0.2$), and therefore it is not surprising that the spectral parameters are very similar.

3.5. The Continuum of ObsID 3815 ($\phi_{\text{orb}} \sim 0.75$)

The analysis of the ~ 45 ks non-dip spectrum of this CC-mode observation is complicated by the lack of imaging information and by calibration issues¹. Below 2 \AA both spectra show an excess of up to $50 \text{ ph cm}^{-2} \text{ s}^{-1} \text{ \AA}^{-1}$ for HEG and up to $150 \text{ ph cm}^{-2} \text{ s}^{-1} \text{ \AA}^{-1}$ in the MEG. This excess is probably caused by contamination of the spectra by the dust scattering halo surrounding the source, which is clearly visible in the detector images of other observations (see also Xiang et al. 2011), or contamination from the wings of 0th order image. As there is no imaging information available in CC-mode, it is not possible to correct for this contamination. Since the low signal-to-noise ratio of the data above 15 \AA does not allow detailed spectral modeling, only the $2-15 \text{ \AA}$ HEG and $2.5-15 \text{ \AA}$ MEG data are taken into account in the further analysis.

Unlike for the TE-mode data, the continuum here cannot be described by the simple power law of Eq. (2), as non-physical curvature caused by calibration issues is present in the spectrum. We model this curvature by adding two non-physical Gaussian components, centered at $\sim 1.12 \text{ keV}$ and $\sim 2.25 \text{ keV}$. Calibration issues causing slope differences between both instruments also necessitated separate modeling of the continua of the HEG and the MEG. The final parameters of the continuum fit are summarized in Table 3.

Note that despite the fact that the broad band CC mode calibration is suboptimal, its relative calibration over small wavelength intervals is still good. This means that parameters of absorption lines can nevertheless be measured. For example, equivalent widths of narrow absorption lines do not depend on the overall shape of the continuum and are therefore not affected by local fitting or the shape of the non-physical continuum model. Since the Ne column is, as in the other observations, obtained mainly from modeling the Ne K-edge, i.e., a local quantity, the Ne column density could be measured independently from the total column.

Table 3. Continuum parameters of ObsID 3815

Parameter	HEG-1	HEG+1	MEG-1	MEG+1
power-law				
A_{PL}	2.70 ± 0.01	2.68 ± 0.01	2.24 ± 0.01	2.53 ± 0.01
Γ	1.81 ± 0.01	1.73 ± 0.01	1.64 ± 0.01	1.69 ± 0.01
tbnew				
$N_{\text{H}} [\text{cm}^{-2}]$	$(0.352^{+0.005}_{-0.003}) \times 10^{22}$			
$N_{\text{Ne}} [\text{cm}^{-2}]$	$(0.76^{+0.01}_{-0.04}) \times 10^{18}$			
gauss $E \sim 1.12 \text{ keV}$ ($\lambda \sim 11 \text{ \AA}$)				
A	0.23	0.17	0.15	0.04
σ	0.178	0.163	0.159	0.099
gauss $E \sim 2.25 \text{ keV}$ ($\lambda \sim 5.5 \text{ \AA}$)				
A	0.03	0.01	0.07	0.04
σ	0.232	0.117	0.283	0.196
χ^2/dof	29805/14406			
χ^2_{red}	2.07			

Notes. A_{PL} – flux density of the power-law at 1 keV in $\text{cm}^{-2} \text{ s}^{-1} \text{ keV}^{-1}$; Γ – photon index of the power-law; A – flux of the broad line feature in $\text{ph cm}^{-2} \text{ s}^{-1}$; σ – line width in keV .

4. Modeling of Line Features

4.1. Introduction

Visual inspection of the non-dip spectra reveals that all spectra show discrete line absorption due to highly ionized material, mostly from H-like and He-like ions of S, Si, Al, Mg, Na, and Ne. We also observe intercombination (i) and forbidden (f) emission lines of He-like ions. Various L-shell transitions of Fe are also present. Table 4 of paper I gives a complete list of transitions from H- and He-like ions present in the spectrum of ObsID 3814 ($\phi_{\text{orb}} \sim 0.95$). Most of these absorption lines are also present in the spectra of ObsID 8525, 9847, and 3815 ($\phi_{\text{orb}} \sim 0.0-0.2$ and $\phi_{\text{orb}} \sim 0.75$). Since the wavelength range used here is smaller than in paper I, lines from O VIII, O VII, Fe XXVI, and Ni XXVIII are outside of the investigated spectral range.

To describe the lines from the H- and He-like ions we fit all transitions of the series from a given ion simultaneously using a curve of growth approach (see paper I for a detailed description of this model). This approach allows us to describe weaker and often blended lines, while their description with separate Gaussian profiles would often be impossible. For each line series, the fit parameters are the column density of the ion responsible for the line, N_i , the Doppler shift, v_i , and the thermal broadening parameter, ξ_i . All line shapes are modeled using Voigt profiles.

In addition to the lines from line series, other absorption and emission lines are also present in the spectra. Where such lines were identified, they were added by hand. Unless noted otherwise, line shapes were described using Voigt profiles, with fit parameters being the thermal broadening parameter, ξ , the natural line width, Γ , i.e., the full width at half maximum of the Lorentzian component of the Voigt profile, and the line flux, A . Negative fluxes denote absorption lines.

The following sections discuss the details and peculiarities of each observation.

4.2. Line spectroscopy of ObsIDs 8525 and 9847

($\phi_{\text{orb}} \sim 0.05$, $\phi_{\text{orb}} \sim 0.2$)

The line identifications for these observations are shown in Figs. A.1 and A.2. While we are able to fit all line series in

¹ http://cxc.harvard.edu/cal/Acis/Cal_prods/ccmode/ccmode_final_doc02.pdf

ObsID 9847, Ar xvii and Ca xix could not be constrained in ObsID 8525. In addition to the absorption lines from H- and He-like ions and Fe, the spectra show evidence for lower ionization absorption lines of Si xii (Li-like), Si xi (Be-like), Si x (B-like), and Si ix (C-like) in the 6.6 Å–7.0 Å band. As we will discuss in greater detail in our analysis of the dip spectrum (Hirsch et al., 2016, in prep.), these features become very strong during the deepest phases of absorption dips. Their appearance in the non-dip spectrum therefore reveals the presence of cooler dense material along the line of sight. This is not surprising given that ObsIDs 8525 and 9847 represent the densest part of the wind, $\phi_{\text{orb}} \sim 0.0\text{--}0.2$, where most dipping is observed. The spectra taken farther away from the superior conjunction, which are far less dominated by dips, are virtually free of lower ionization Si features, with the exception of possible detections of a Si xii line in ObsID 11044 ($\phi_{\text{orb}} \sim 0.5$) and a Si xi line in ObsID 3815 ($\phi_{\text{orb}} \sim 0.75$). We note, however, that in all cases the optical depth of the lines is much smaller than that seen during dips and consider our results to be representative of the non-dip spectrum. Best-fit line parameters of the Si features are listed in Table 4. Note that Si xii $\lambda 6.72$ Å blends with Mg xii Ly γ and the Si xiii f emission line, while Si xi $\lambda 6.785$ Å blends with a line from Fe xxiv. The parameters of these lines are therefore difficult to constrain².

Si xiii forbidden line at 6.74 Å is a single emission feature in the spectrum and its modeling is ambiguous due to possible blends described above. Fixing Γ and fitting the feature gives line fluxes of $0.29^{+0.15}_{-0.13} \times 10^{-3} \text{ ph s}^{-1} \text{ cm}^{-2}$ in ObsID 8525 and $0.56 \pm 0.16 \times 10^{-3} \text{ ph s}^{-1} \text{ cm}^{-2}$ in ObsID 9847, while the thermal broadening parameter, ξ , is almost unconstrained.

4.3. Line spectroscopy of ObsID 3815 ($\phi_{\text{orb}} \sim 0.75$)

The full range spectrum is given in Fig. A.3. In this observation, the line series of Ar xvii, Ca xix, Ca xx and Fe xvii could not be fitted. The approach of line series fitting does not allow us to describe every single line perfectly, but this is mostly only the case for weak emission lines or Fe blends. Notable is the discrepancy in the case of Ne x. If Ne x Ly α (12.13 Å) is modeled properly, then Ne x Ly β (10.24 Å), Ne x Ly γ (9.71 Å), and Ne x Ly δ (9.48 Å) are predicted to be weaker than observed. To find the reason for this discrepancy, we excluded a very narrow region of the spectrum where the Ne x Ly α is located and fitted the spectrum without this line. All other lines of the Ne x series were described very well. There is, however, no reason to assume that the data in the region of Ne x Ly α are of low quality, especially not for non-dip spectra with their good statistics, and this discrepancy is probably due to contamination by nearby Fe lines. Ne x Ly α also appears to be asymmetric, possibly being an indication of P Cygni profiles (see Sect. 4.4). Miller et al. (2005)³ reported inconsistencies in equivalent widths between individual lines in the Ne x series. Apart from (partial) saturation of the resonance line or blends of lines, the authors argued that another possible explanation would be that lines come from an inhomogeneous region, or from different regions simultaneously. Marshall et al. (2001)⁴ described an opposite problem,

Table 5. Intercombination (i) and forbidden (f) emission lines from He-like ions at $\phi_{\text{orb}} \sim 0.75$ (ObsID 3815)

	λ [Å]	A [$10^{-3} \text{ ph s}^{-1} \text{ cm}^{-2}$]	ξ [km s^{-1}]
Ne ix f	13.726	0.12 ± 0.09	≤ 200
Ne ix i	13.561	$0.59^{+0.09}_{-0.10}$	140^{+70}_{-100}
Na x f	11.199	$0.61^{+0.18}_{-0.31}$	590^{+370}_{-90}
Na x i	11.089	$0.84^{+0.62}_{-0.19}$	1200^{+2600}_{-500}
Mg xi f	9.316	$0.17^{+0.07}_{-0.06}$	≤ 200
Mg xi i	9.235	0.47 ± 0.07	≤ 180
Al xii f	—	—	—
Al xii i	7.81	0.4 ± 0.08	550^{+200}_{-150}
Si xiii f	6.742	$0.79^{+0.05}_{-0.07}$	< 149
Si xiii i	6.685	$0.27^{+0.08}_{-0.07}$	360^{+140}_{-310}
S xv f	—	—	—
S xv i	5.054	$0.05^{+0.09}_{-0.05}$	≤ 200

Notes. Full width at half maximum, Γ , was fixed to 15 eV for the lines indicated in **bold**. For all the other lines, it was fixed to 1.5 eV. Emission lines of Ar xvii and Ca xix were not present in the spectrum.

that while the Ly α lines were strong, no Ly β lines were detected, concluding that the lines were not saturated and that the absorbing gas covered more than $\sim 50\%$ of the source.

Emission lines are present in the spectrum but are generally much weaker than the absorption lines. Since full width at half maximum, Γ , and the thermal broadening, ξ , of the line are correlated for Voigt profiles, it was difficult to constrain their parameters (Table 5). We therefore set Γ to a fixed value that is located at the intersection of the confidence contours for all individual emission lines from the free fits, which appeared to be split into two groups: for stronger lines, Γ was fixed to 15 eV and the thermal broadening reaches values around $\sim 500 \text{ km s}^{-1}$. The full width at half maximum of the weaker lines was fixed to 1.5 eV and ξ is mostly consistent with zero.

4.4. Line spectroscopy of ObsID 11044 ($\phi_{\text{orb}} \sim 0.5$)

Whereas resonance transitions were always detected in absorption at early orbital phases, the spectrum at $\phi_{\text{orb}} \sim 0.5$, taken during the inferior conjunction of the black hole, shows P Cygni profiles with an emission component at the rest wavelength and a weak blue-shifted absorption component. Due to the complex profiles, in this observation line series fitting is not feasible. Describing the P Cygni profiles as the sum of a positive and a negative Voigt profile allows us to model the shapes of the Ly α transitions of Si xiv, Mg xii, and Ne x, Ne x β and δ quite well (Table A.2). In addition, the data show the Mg xi triplet, four pure emission lines, and only two pure absorption lines. See Fig. A.4 for the full spectrum.

Although the interpretation of P Cygni profiles is challenging, we attempt to determine column densities for the absorption part of the profiles using (Mihalas 1978, see also paper I)

$$N_i = \frac{mc^2 W_\lambda}{\pi e^2 \cdot f_{ij} \lambda_0^2} = \frac{1.13 \times 10^{17} \text{ cm}^{-2}}{f_{ij}} \cdot \left(\frac{\lambda_0}{\text{Å}} \right)^{-2} \cdot \left(\frac{W_\lambda}{\text{mÅ}} \right), \quad (3)$$

assuming that the lines are not saturated ($\tau(\nu) \ll 1$). Here, W_λ is the equivalent width of the line, and f_{ij} is the oscillator strength of the transition, in this case a sum of all transitions contributing to the absorption line. The values of N_i are summarized in Table A.2. Column densities for Ne x β and δ are outliers. Values of ~ 75 and $\sim 85 \times 10^{16} \text{ cm}^{-2}$ are far too high given the column

² Because of blends, the Si absorption lines visible in the non-dip spectrum of ObsID 3814 were not identified as such in Fig. 10 of paper I.

³ ObsID 2415: ~ 32 ks at $\phi_{\text{orb}} \sim 0.76$, CC mode, \sim twice as high flux as common

⁴ ObsID 1511: 12.7 ks at $\phi_{\text{orb}} \sim 0.84$, CC mode

Table 4. Low ionization Si lines in ObsIDs 8525 ($\phi_{\text{orb}} \sim 0.05$) and 9847 ($\phi_{\text{orb}} \sim 0.2$)

Line	λ_{lab} [Å]	ObsID	λ_{obs} [Å]	A [$10^{-4} \text{ ph s}^{-1} \text{ cm}^{-2}$]	Δv [km s^{-1}]	ξ [km s^{-1}]
Si XII (Li)	6.7200 ± 0.0003	8525	6.716 ± 0.004	$-3.4^{+1.0}_{-1.2}$	-162 ± 162	130^{+320}_{-100}
		9847	6.715 ± 0.003	-5.9 ± 1.3	-244 ± 114	380^{+200}_{-220}
Si XI (Be)	6.7848 ± 0.0003	8525	line not present			
		9847	6.7750 ± 0.0001	$-3.2^{+0.8}_{-0.9}$	-434 ± 7	15^{+334}_{-4}
Si X (B)	6.8565 ± 0.0002	8525	6.858 ± 0.008	$-2.7^{+1.2}_{-1.3}$	43 ± 332	600^{+600}_{-500}
		9847	6.859 ± 0.001	$-1.2^{+1.3}_{-1.4}$	126 ± 33	≤ 2595
Si IX (C)	6.9285 ± 0.0003	8525	6.9228 ± 0.0001	-11^{+11}_{-15}	248 ± 2	≤ 749
		9847	line not present			

Notes. λ_{lab} : laboratory wavelength (Hell et al. 2013), λ_{obs} : observed wavelength, A: line flux (negative: absorption), Δv : velocity shift, ξ : thermal broadening parameter.

density of $\text{Ne x}\alpha$. This deviation is most likely due to a partial filling of the absorption component by the strong emission wing, which cannot be determined reliably due to the low signal-to-noise ratio of the line (Fig. A.4). Columns were also determined for the absorption line at $\lambda 6.705 \text{ Å}$ assuming it is from Li-like Si XII, using the oscillator strength of Behar & Netzer (2002).

The fact that the columns of the absorption lines are much smaller in this observation compared to earlier orbital phases demonstrates that the column density of the ionized absorber is strongly modulated with orbital phase, although the blending of the absorption and the emission component strongly influences the interpretation of the columns found for this observation. A more detailed study would require fits of P Cygni profile models using line profile shapes in which the exciting source is not situated at the center of the complex, asymmetric flow. To our knowledge, such calculations are not available so far.

Doppler shifts, v_i , of the absorption and the emission components of the P Cygni profiles were determined separately (Table A.2). As the emission components are located rather close to the rest wavelength and, except for lines from Ne x , are redshifted, and the absorption tails are, in contrast, strongly blueshifted, they provide only upper/lower limits of the velocity values.

4.5. Line spectroscopy: Best-fit results

Figure 4 shows the parameters of individual line series summarized in Table A.1: Doppler velocities v_i , column densities N_i and thermal broadening ξ_i for ObsIDs 8525, 9847, and 3815 ($\phi_{\text{orb}} \sim 0.0$ – 0.2 and 0.75). Parameters obtained in paper I from ObsID 3814, $\phi_{\text{orb}} \sim 0.95$, are shown for comparison. Due to the different fitting approach, the parameters of ObsID 11044 ($\phi_{\text{orb}} \sim 0.5$) are excluded from this comparison.

All series in ObsID 3815 ($\phi_{\text{orb}} \sim 0.75$) are consistently redshifted, with values falling in the interval between 100 and 400 km s^{-1} . The exception is the Na x line, which is Doppler shifted by $\sim 870 \text{ km s}^{-1}$. The column densities of all line series (Fig. 4) are in the interval $(0\text{--}5) \times 10^{16} \text{ cm}^{-2}$ with a thermal broadening of $\xi \lesssim 500 \text{ km s}^{-1}$, suggesting the lines originate from the same region.

Because of the short exposure of ObsIDs 8525 and 9847, many fit parameters show large uncertainties or cannot be constrained. The velocities in ObsIDs 8525 and 3814 ($\phi_{\text{orb}} \sim 0.0$) are much lower compared to ObsID 3815, in fact, they are consistent with zero, while the ones from ObsID 9847 ($\phi_{\text{orb}} \sim 0.2$) show mostly blueshifted values. Overall, the velocities span the range $\pm 500 \text{ km s}^{-1}$.

The column densities of ObsIDs 8525, 9847, and 3814 are much higher than those of ObsID 3815, supporting the idea of the denser focused wind around $\phi_{\text{orb}} \sim 0.0$. We do not see any particular trend in the thermal broadening measured in these observations, although with $\lesssim 300 \text{ km s}^{-1}$ it seems to be generally lower than in ObsID 3815 (even though the broadening shows a rather large scatter). For a plasma with a temperature of $T \sim 10^6 \text{ K}$, thermal velocities are on order of $\sim 10 \text{ km s}^{-1}$. The higher observed values therefore suggest that most of the broadening is due to microturbulence.

Closer investigation shows that for lines with lower signal-to-noise a higher column appears to imply smaller thermal broadening. Such behavior could explain the outlier lines. For example, in the case of Si XIV in ObsID 8525 assuming a typical value of $\xi \sim 300 \text{ km s}^{-1}$ would reduce the column density by a factor of ~ 10 . For other lines this effect will be smaller.

5. The X-ray Orbital Variability of Cyg X-1

Having described the properties of the individual observations, we now turn to looking at them in the context of the different lines of sight onto the black hole in order to understand better how the properties of the wind depend on the orbital phase. We first study the variation of the column density obtained from continuum or edge modeling with orbital phase and then investigate the variation of the ionizing absorber by looking at column densities and velocity shifts of individual line series.

5.1. Column density variation of the neutral absorber

The equivalent hydrogen column density N_{H} found from continuum fitting is in principle a tracer for the material in the interstellar medium along the line of sight to the X-ray source and for the moderately ionized material in its vicinity. The reason is that $0.5\text{--}10 \text{ keV}$ X-rays are mainly absorbed by K-shell electrons. As the cross section of the K-shell is only mildly dependent on ionization stage, absorption in moderately ionized material can usually also be described reasonably well with cross sections for neutral atoms, at least at the level that is usually used when modeling broad band continua. N_{H} is thus a measure for both the ISM foreground absorption and the column of mildly ionized material in the stellar wind. Earlier monitoring, e.g., with RXTE, showed a modulation of N_{H} with orbital phase (Grinberg et al. 2015; Hanke 2011; Wilms et al. 2006; Kitamoto et al. 2000; Holt et al. 1976), although we note that some of the modulation seen there is also caused by dips, which were not removed in these analyses.

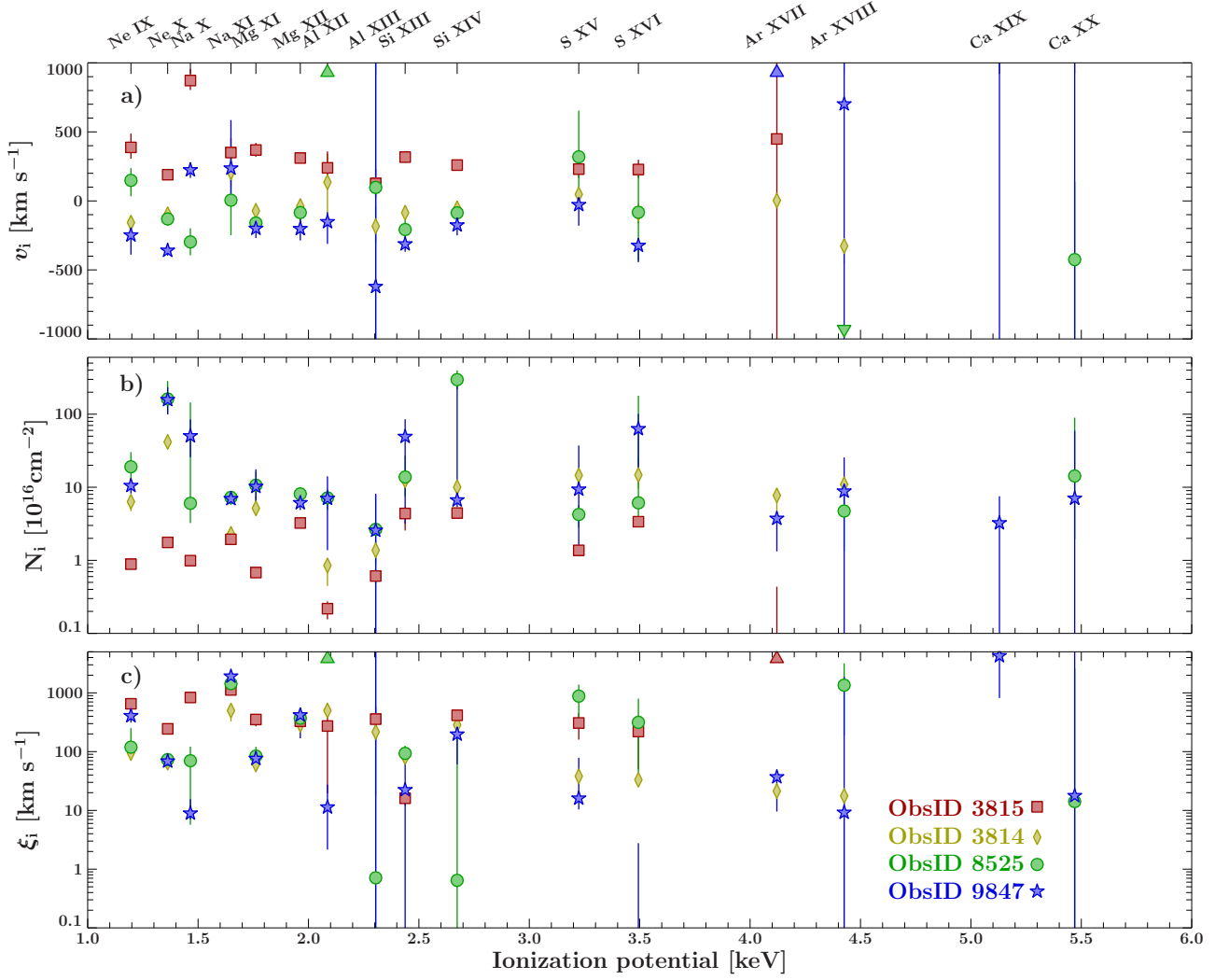


Fig. 4. Fit parameters from Table A.1 for line series of H-like and He-like transitions in ObsID 3815 (squares), ObsID 8525 (circles), ObsID 9847 (stars) and also ObsID 3814 (diamonds, paper I): *top*: velocity shifts, *middle*: column densities, *bottom*: thermal broadening. Colors correspond to ObsIDs as indicated. For completeness, values far above or below the displayed range are marked by triangles close to upper/lower x -axes.

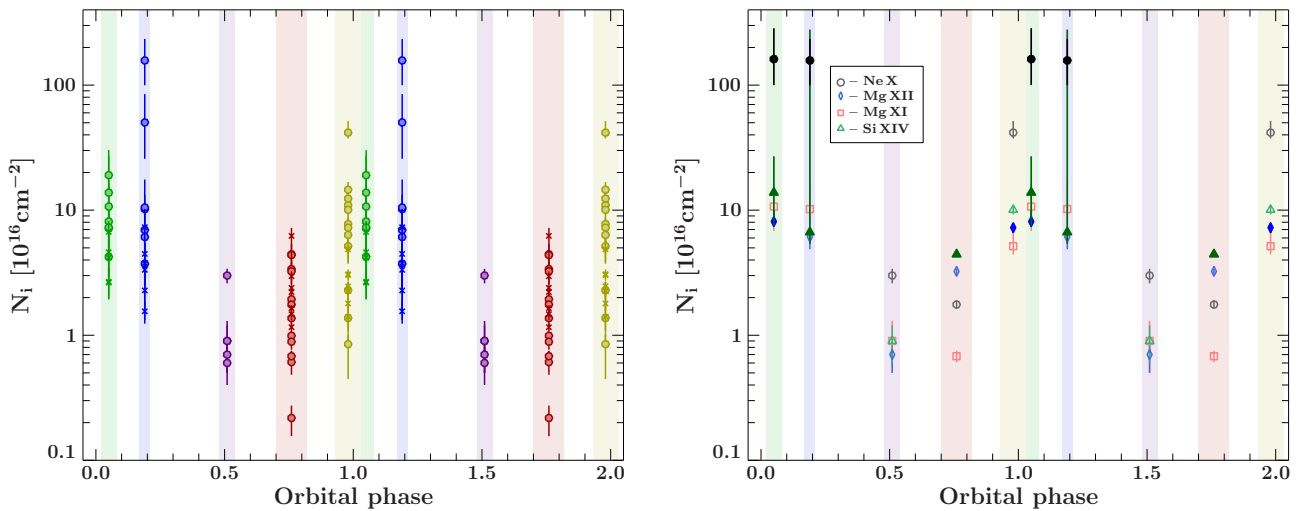


Fig. 6. Measured column densities, N_i , of individual elements as a function of orbital phase. *Left*: H- and He-like line series (circles) and Fe lines (crosses). Only measurements with relative uncertainties $<75\%$ are included. *Right*: Column densities of the four most prominent ions, Ne x (circles), Mg xii (diamonds), Mg xi (squares), and Si xiv (triangles). Filled datapoints correspond to symmetric lines (see Fig. 12 and related discussions).

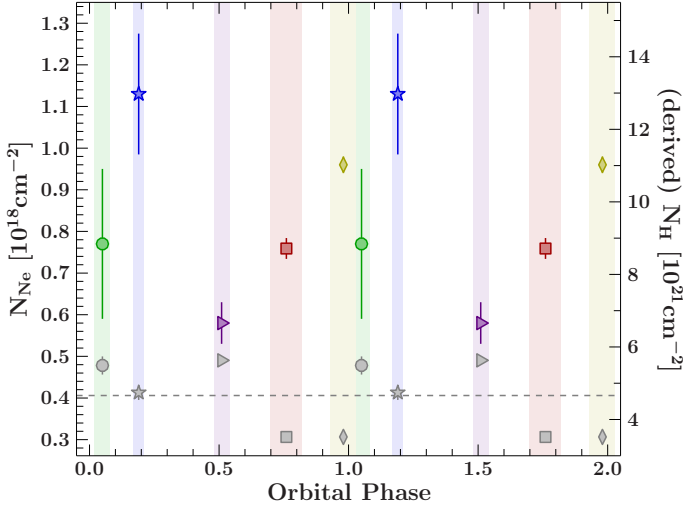


Fig. 5. Orbital phase variation of fitted columns, repeated twice for clarity. Grey data points show the equivalent hydrogen column density, N_{H} , from continuum fitting the *Chandra* spectra (right hand y-axis). As discussed in the text, the data points are heavily influenced by systematics (the error bars shown are statistical only). The colored data points show the variation of the Ne neutral column from Ne-edge fitting (left y-axis) and corresponding N_{H} (right y-axis) derived assuming a Ne:H abundance of 1:11481 as per Wilms et al. (2000). The phases of individual *Chandra* observations are denoted with colored regions. The dashed lines represent the total equivalent column density of the interstellar medium and of Ne (Xiang et al. 2011).

The values obtained from the *Chandra* continuum fitting for the N_{H} (Fig. 5, grey data points) show a systematic offset compared to other determinations of the column, with lowest values of $(3.52^{+0.05}_{-0.03}) \times 10^{21} \text{ cm}^{-2}$ at $\phi_{\text{orb}} \sim 0.75$ and $(3.52 \pm 0.04) \times 10^{21} \text{ cm}^{-2}$ (paper I) for $\phi_{\text{orb}} \sim 0.95$. These values are smaller than the total column density of the interstellar medium along the line of sight to Cyg X-1, which dust scattering measurements determine to $N_{\text{H, tot}} \sim 4.6 \times 10^{21} \text{ cm}^{-2}$ (Fig. 5, dashed line; Xiang et al. 2011). This column sets the lower limit to the total N_{H} to Cyg X-1, which is the sum of the intrinsic absorption in the system and the absorption in the interstellar medium. Lower N_{H} values, as those seen here, thus indicate a systematic error. This is not unlikely, when considering that the lowest N_{H} values originate from an observation performed in continuous clocking mode, where the continuum has to be modeled with additional broad Gaussians (Table 3). A further systematic is the inability to constrain the continuum with *Chandra* in these absorption line dominated data. Our experience shows that fits to simultaneous *Chandra* and *RXTE*-PCA data indeed have significantly higher N_{H} . For example, in paper I we found for observation 3814 that N_{H} increased from $3.52 \pm 0.04 \times 10^{21} \text{ cm}^{-2}$ in the *Chandra*-only fits to $N_{\text{H}} = 5.4 \pm 0.4 \times 10^{21} \text{ cm}^{-2}$ when including the PCA data, consistent with previous measurements (Miller et al. 2002; Schulz et al. 2002) and also with the N_{H} obtained from continuum fitting to observation 8525, which has a similar orbital phase. We therefore conclude that N_{H} values obtained from continuum modeling the *Chandra* data alone suffer a large systematic uncertainty in these line dominated data, with a clear systematic bias towards smaller N_{H} .

An independent, and likely better, measure for the absorbing column is possible by direct measurement of the optical depth at absorption edges. This approach is less dependent on systemat-

ics of the continuum modeling than fitting N_{H} , especially considering the systematics induced by the brightness of the source. In our data, Neon is the only element for which we can measure the column density directly from the neutral edge in all of our observations (Fig. 5, colored data points). The observed variation suggests that part of the neutral N_{Ne} is intrinsic to the source and varies with orbital phase, with a minimum at $\phi_{\text{orb}} \sim 0.5$, consistent with earlier studies of the N_{H} variation in the system (e.g., Grinberg et al. 2015; Wen et al. 1999; Kitamoto et al. 2000). We note, however, that a potential systematic uncertainty is that only ObsID 11044 ($\phi_{\text{orb}} \sim 0.5$) does not show any significant absorption lines in the range of the Ne edge, while for the other ObsIDs this region is populated by many strong lines from ionized Fe. It therefore cannot be excluded that some of the variation is due to a contamination of the Ne edge by these lines. A cross check in which the continuum around the Ne edge is modeled locally reveals columns that are systematically higher by a factor of ~ 2 , such that at least part of the modulation could be due to the Fe lines. Local and continuum modeling give similar results only for ObsID 3815 ($\phi_{\text{orb}} \sim 0.75$). In addition to Ne, the good quality of ObsID 11044 ($\phi_{\text{orb}} \sim 0.5$) allows us to leave the Fe column a free parameter in the continuum fitting, giving $N_{\text{Fe}} = (0.15 \pm 0.02) \times 10^{18} \text{ cm}^{-2}$ for this observation. This value is consistent with N_{Fe} determined from the local modeling of the edge and with the expected ISM Fe contribution using the ISM abundances of Wilms et al. (2000).

5.2. Orbital variation of the column of the ionized absorber

We now turn to the variation of the ionized absorber with phase. Figure 6 illustrates the variation of the column densities N_i of highly ionized elements with orbital phase. The parameter sample was reduced compared to the complete set of species present in the spectra by excluding all columns with uncertainties exceeding 75% of their values. For ObsIDs 3814 and 3815 ($\phi_{\text{orb}} \sim 0.95$ and 0.76) only one N_i value per observation, from S xvi and Ar xvii, respectively, was lost. For ObsIDs 8525 and 9847 ($\phi_{\text{orb}} \sim 0.05$ and 0.2 , ~ 4.4 ks exposure) we discarded roughly half of the N_i values (ObsID 8525, $\phi_{\text{orb}} \sim 0.05$: H-like series of Ne, Al, Si, S, Ar and Ca, and He-like Na; ObsID 9847, $\phi_{\text{orb}} \sim 0.2$: both H- and He-like series of Al, Si, S, Ca, and H-like Ar). Figure 4b shows that these N_i values are, to within their uncertainties, consistent with the more tightly constrained values. Ne x and Na x of ObsID 9847 ($\phi_{\text{orb}} \sim 0.2$) appear as outliers, although compared to other columns determined in this observation they are relatively well constrained. In ObsID 11044 ($\phi_{\text{orb}} \sim 0.5$), where the strong lines show P Cygni profiles, the N_i shown in Fig. 6 were determined as described in Sect. 4.4 for the absorption parts of Ne x α , Mg xii, Mg xi, and Si xiv.

There are four ions that are strong in all five observations and so can be tracked over the whole orbit: Ne x, Mg xii, Mg xi, and Si xiv (Fig. 6, right). On closer investigation the lines appear asymmetric even in cases where they do not show clear P Cygni profiles. As asymmetry can affect the column density measurements, we considered only those lines which do not show any asymmetry according to Sect. 6.1 (filled circles in Fig. 6). Similarly to the cases discussed above, N_i is expected to reach its maximum at $\phi_{\text{orb}} \sim 0.0$ and its minimum at $\phi_{\text{orb}} \sim 0.5$. The modulation is clearly visible in Fig. 6.

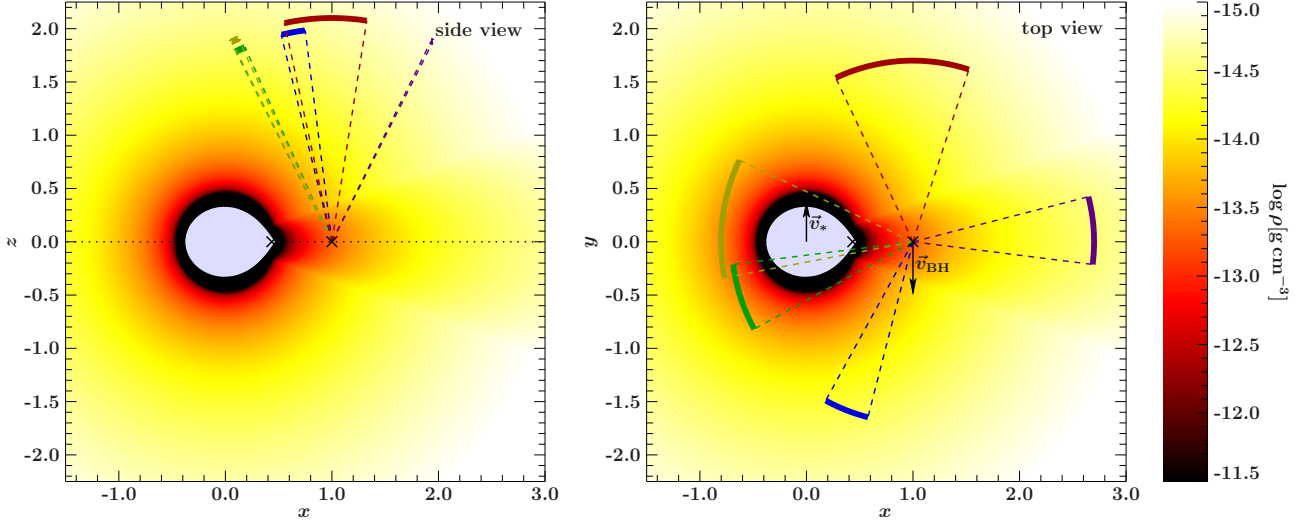


Fig. 7. Stellar wind density assuming the focused wind model of Gies & Bolton (1986) and lines of sight towards the black hole. *Left:* Side view onto the orbital plane (dashed). *Right:* Lines of sight projected onto the orbital plane. The black hole (cross) and its donor move clockwise around the center of mass (cross).

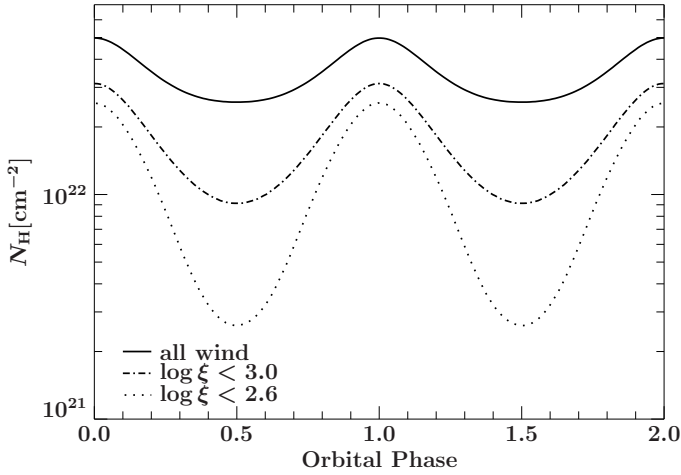


Fig. 8. Phase variation of the column density according to the focused wind model of Gies & Bolton (1986). Shown is the column of the whole wind (solid line), and of those less ionized wind regions where the ionization parameter $\log \xi < 3.0$ (dash dotted line) and $\log \xi < 2.6$ (dotted line), respectively.

5.3. The location of the absorbers

The previous sections showed that both, the moderately ionized material tracked by Ne-edge fitting and the highly-ionized material responsible for the H- and He-like species shows orbital modulation, i.e., the material is local to the X-ray binary. In this Section we consider the relationship between both absorbers. First, as also pointed out by Marshall et al. (2001), note that in most observations the He-like line series show lower columns than their H-like peers, $N_{i,\text{He}} \leq N_{i,\text{H}}$ (Fig. 4), which indicates that most of the material traced by the H- and He-like lines is fully ionized. The best example in this respect is ObsID 3815, where for all observed line series the column of the H-like ions is larger than the column from the He-like ions. In this ObsID, $\phi_{\text{orb}} \sim 0.75$, i.e., the line of sight is almost perpendicular to the binary axis. For the other observations probing the denser part of the wind, the relation between $N_{i,\text{He}}$ and $N_{i,\text{H}}$ is not as clear as for ObsID 3815, but $N_{i,\text{He}} \leq N_{i,\text{H}}$ is fulfilled for most ions.

To compare the measured variation of the columns with theoretical expectations we use the focused wind model of Gies & Bolton (1986) as a toy model. This model consists of a CAK-model with a longitudinal variation of the wind parameters in a cone $\pm 20^\circ$ degrees from the line between the donor and the black hole. Outside of that region we use the wind parameters at $\theta = 20^\circ$, where θ is the angle in the orbital plane of the binary, measured from the line between the donor and the black hole. Figure 7 shows the density structure of the focused wind as well as the line of sight of our observations projected onto the orbital plane and in a side view. The model has been shown to be a good overall representation of the stellar wind in the HDE 226868/Cyg X-1 system, even though the detailed parameters of the wind are still debated (Gies et al. 2003; Gies et al. 2008; Vrřilek et al. 2008, and references therein). We emphasize that much of this discussion relates to the wind properties in the so-called “shadow wind”, i.e., the region of the star opposite to the black hole where X-rays are not presumed to influence the wind properties (Caballero-Nieves et al. 2009). This region is not probed by the line of sights studied here.

Figure 8 (solid line) shows that in the model of Gies & Bolton (1986) the total (neutral and ionized) column is around $N_{\text{H}} \sim 4 \times 10^{22} \text{ cm}^{-2}$, i.e., it is more than a factor of 10 higher than the N_{H} measured from fitting the continuum or the N_{H} values inferred from fitting the Ne edge. The latter vary between $6.8 \times 10^{21} \text{ cm}^{-2}$ and $1.3 \times 10^{22} \text{ cm}^{-2}$ (Fig. 5). Due to the expected high degree of ionization caused by the black hole and the UV radiation from its donor, this difference between the measured N_{H} and the model predicted total columns is not surprising (e.g., Holt et al. 1976; Wen et al. 1999). Figure 8 therefore also shows the expected columns from regions where the ionization parameter, $\log \xi$, is < 3 and < 2.6 . Following Tarter et al. (1969), we define the ionization parameter as $\xi = L/(nr^2)$, where L is the source luminosity above the hydrogen Lyman edge, n is the absorbing particle density and r is the distance from the ionizing source. We will be using $L = 10^{37} \text{ erg s}^{-1}$ throughout, a typical value for our observations when taking into account the UV and $> 10 \text{ keV}$ emission of the source (Table 1). Similar to Wen et al. (1999) we also ignore the contribution of the UV photons from the donor star, which systematically increases the ionization parameter. Numbers quoted in the following are therefore to be

considered lower limits. Note that we use the symbol ξ for both, the ionization parameter and the thermal broadening parameter in line series fitting. We do not anticipate confusion because they are used in different contexts.

Figure 8 indicates that the modulation of the absorption found in the Ne edge and in line series (Figs. 5 and 6) is in qualitative agreement with the variation expected due to the moderately ionized region of the wind, i.e., where $\log \xi < 2.6$. This is the outermost region of the wind (for $r \rightarrow \infty$, $\log \xi \rightarrow 2.5$), i.e., consistent with the observational findings most of the wind is expected to be ionized. With a variation by a factor of ~ 2 , however, the total expected variation in the model of Gies & Bolton (1986, Fig. 8, solid line) is at the lower end of what is found in the observations, where we found a variation of a factor of ~ 2 for tracers of the neutral column (Fig. 5, colored data points) to a factor of ~ 10 for the highly ionized species (Fig. 6). In addition, comparing the expected variation at low $\log \xi$ with the total column, based on Fig. 8 we would expect ionized columns that are only a factor of a few larger than the neutral column, while for most ions the difference in the data is higher. It is unlikely that all of this discrepancy is due to the simplifications of the wind model of Gies & Bolton (1986) alone. We note, however, that we used the interstellar abundances to convert the overall continuum N_H values to columns for the individual ions. This is probably not correct, since an evolved star such as HDE 226868 is likely to show a different abundance pattern. Assuming that the most important metals are overabundant with respect to the interstellar medium, the difference could be explained. Overabundances in Cyg X-1 were reported previously. Modeling the emission $K\alpha$ line, Duro et al. (2011) and Fabian et al. (2012) determined the Fe abundance in the accretion disk to be $1.2\text{--}1.6A_{\text{Fe}\odot}$. Further analysis gives much higher values of $A_{\text{Fe}} \sim 3\text{--}6A_{\text{Fe}\odot}$ (Duro et al. 2016). Reflection modeling also yields an iron overabundance of $1.9\text{--}2.6$ (Tomsick et al. 2014). Independent of X-ray measurements, the analysis of optical and UV spectra of HDE 226868 also yields a nitrogen overabundance of five times solar (Caballero-Nieves et al. 2009). This result also suggests the possibility of the other elements being overabundant, which is not so surprising, given that the system consists of an evolved star and has experienced a supernova.

We therefore conclude that a large fraction of the observed medium is ionized and that it is very likely that the observed wind volume is enriched in metals. Since the medium is ionized, it is located fairly close to the black hole. Depending on the line of sight, the distance from the black hole within which $\log \xi > 2.6$ is between $0.5d$ and $3.6d$, where d is the distance between the donor and the black hole. To constrain the properties of the absorber further, we therefore need to turn to another observable, the Doppler shift of the observed lines.

Figure 9 shows that there is a systematic sinusoidal modulation of the velocity shifts of individual line series from the ionized absorber with orbital phase. Velocities for ObsID 11044 at $\phi_{\text{orb}} \sim 0.5$ are systematically shifted to lower velocities because here only the absorbing part of the P Cygni profile was taken into account. We therefore ignore this observation for the remainder of our discussion.

At a first glance, the line shifts appear to be approximately in phase with the radial velocity of the black hole, which has a velocity amplitude of $K_{\text{BH}} \sim 98 \text{ km s}^{-1}$ (Orosz et al. 2011) and a systemic velocity of $v_0 = -7.0 \pm 0.5 \text{ km s}^{-1}$ (Gies et al. 2003). We performed a set of fits to establish whether the wind follows the black hole, and investigated several different scenarios (Table 6): we used all line series shown in Fig. 9 including ve-

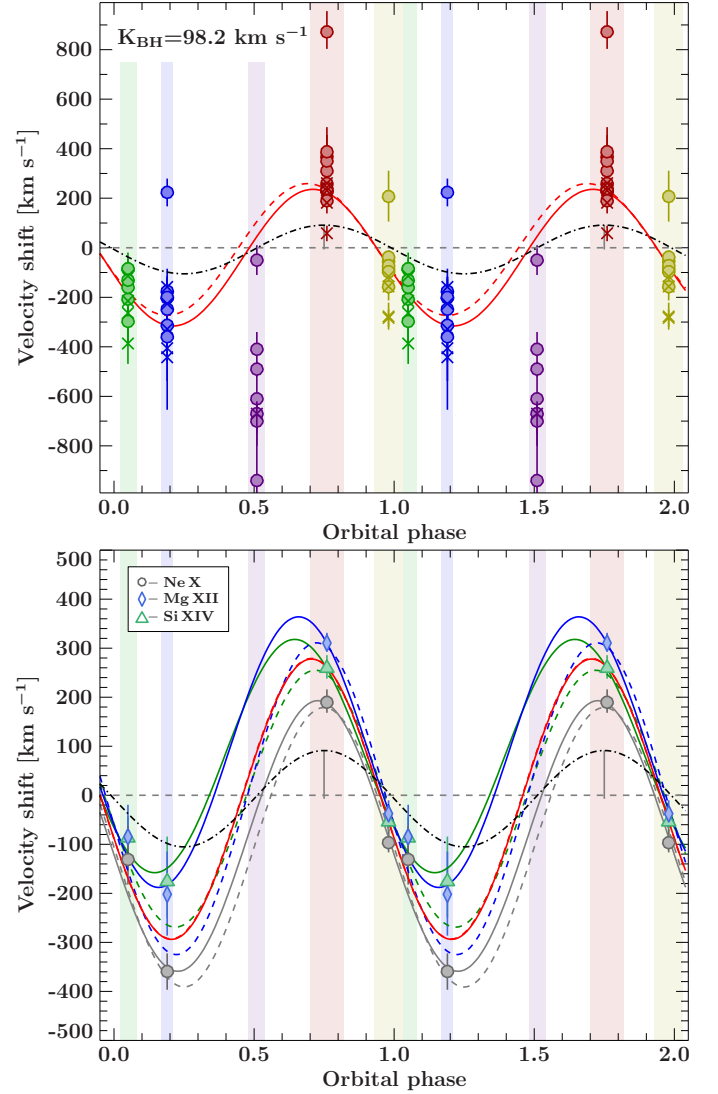


Fig. 9. *Top:* Velocity shifts of individual line series (circles: H-like and He-like ions, crosses: Fe line series) and the radial velocity of the black hole (dash-dotted line, semi-amplitude of $\sim 98 \text{ km s}^{-1}$). The red sine curve shows the best fit involving all series shown ($K_W \sim 276 \text{ km s}^{-1}$, $v_0 \sim -40 \text{ km s}^{-1}$, and $\Delta\phi \sim 0.46$), while the dashed line shows the “second best fit” where the offset was fixed to the systemic velocity of the black hole (Table 6). *Bottom:* Velocity shifts for individual ions and the radial velocity of the black hole (dash-dotted line). The sine curves represent the best fits for each of the three given line series (Table 6). Dashed lines show fits with the offset fixed to the systemic velocity of the black hole. The red sine curve is the best fit involving all three line series (Table 6).

locities from ObsID 11044, $\phi_{\text{orb}} \sim 0.5$, the lines of Ne x, Mg xii, Si xiv together, and each of these three lines individually. Apart from a fit in which all parameters of the sine were left free, we also constrained the fits to be in phase with the black hole and to have a different amplitude than the black hole. Generally, models with varying phase shifts give better results than those with the zero phase shifts (bold rows in Table 6). The velocities of different ions are clearly not consistent with each other, indicating a complex ionization structure.

We contrast these results in Fig. 10 with the radial velocities expected from the focused wind model of Gies & Bolton (1986).

Table 6. Sine function parameters describing the orbital modulation of the Doppler shifts. The fits are to a model of the form $v(\phi) = v_0 + K_W \cdot \sin[2\pi(\phi - \Delta\phi)]$. Parameters without uncertainties were held fixed in the fit.

K_W [km s ⁻¹]	v_0 [km s ⁻¹]	$\Delta\phi$	χ^2/dof	χ^2_{red}
all lines included in Fig. 9:				
276 ± 11	-40 ± 14	0.073 ± 0.002	428.28/34	12.59
242 ± 10	-7	0	539.01/36	14.97
266 ± 10	-7	0.070 ± 0.002	433.93/35	12.39
297 ± 11	-84 ± 8	0	442.79/35	12.65
fit to Ne x, Mg xii, and Si xiv:				
286⁺²⁵₋₂₄	-8 ± 36	0.072 ± 0.004	30.87/9	3.43
271 ± 19	-7	0	63.45/11	5.77
286 ± 20	-7	0.072 ± 0.002	30.9/10	3.09
313 ± 24	-62 ± 18	0	39.07/10	3.91
fit to Ne x:				
276 ± 37	-83 ± 48	0.076 ± 0.006	1.72/1	1.72
236 ± 33	-7	0	41.24/3	13.75
267 ± 34	-7	0.067 ± 0.003	8.49/2	4.24
285 ± 36	-106 ± 26	0	2.67/2	1.33
fit to Mg xii:				
276⁺⁴⁷₋₃₈	88 ± 91	0.07 ± 0.01	0.48/1	0.48
309 ± 30	-7	0	7.67/3	2.56
318 ± 32	-7	0.075 ± 0.003	3.46/2	1.73
334 ± 47	-33 ± 38	0	6.39/2	3.19
fit to Si xiv:				
238⁺⁴⁸₋₄₁	80 ± 89	0.063 ± 0.013	0.69/1	0.69
256 ± 38	-7	0	6.79/3	2.26
262 ± 38	-7	0.075 ± 0.004	3.31/2	1.65
275 ± 48	-30 ± 37	0	5.74/2	2.87

Notes. K_W – amplitude of the sine curve; v_0 – offset of the sine curve, $\Delta\phi$ – phase shift: $v_0 = -7 \text{ km s}^{-1}$ and $\Delta\phi = 0$ are fixed to the orbital motion of the black hole. Best fits are printed in **bold**.

A direct fit of the ion velocities to this model is not justified, the figure therefore indicates the typical range for the Doppler shifts of our observations. The projected wind velocities for the range of distances in which the highly ionized lines originate according to our analysis of the columns is in agreement with the measured shifts. Note, however, that the wind model predicts a phase shift of $\Delta\phi = 0.25$ between the black hole and the wind, different from what is seen. The measurements during phase 0 are consistent with an origin $\leq 0.25d$ from the black hole (as before, d is the distance between the donor and the black hole), while the data taken during phase 0.75 are consistent with a distance $\leq 0.5d$. Given that this observation is the brightest of our observations, it is not unexpected that the ionized region should move away from the black hole. The overall redshift measurements therefore agree with our conclusion that the ionized absorber must originate close to the black hole, and possibly in the focused wind.

While the data from observations 3814, 3815, and 8525 could originate in the focused wind, ObsID 9847 presents an interesting outlier. During this observation the absorbing material appears to be moving towards the observer with a blueshift that is much higher than that of the black hole. As shown in Fig. 10, except for a region very close to the black hole, only positive radial velocities (=redshifts) are expected during this observation. To reconcile these data with a focused wind would require terminal velocities of $> 4500 \text{ km s}^{-1}$. This value is much higher than the $\sim 2500 \text{ km s}^{-1}$ typically assumed for the wind at the location of the black hole (this value decreases for stream lines

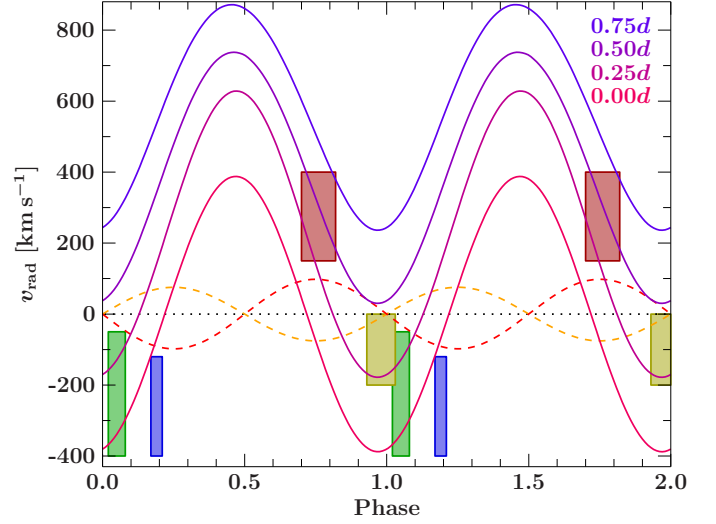


Fig. 10. Radial velocities of the black hole (red dashed line) and of HDE 226868 (orange dashed line) and wind velocities projected onto the line of sight as a function of distance from the black hole. Distances are given in units of the distance between the black hole and its donor, a . Colored boxes indicate the range of the measured Doppler shifts from the *Chandra* observations, excluding ObsID 11044.

away from the line of symmetry of the system). As an alternative explanation we note that during this observation we are looking through the “bow shock” of the black hole (e.g., Manousakis 2011; Blondin & Woo 1995, and references therein), i.e., a region where the wind is strongly disturbed. It is not unlikely that in this region material gets so disturbed that it obtains a significant non-radial velocity, which at this phase would show up as a high blue shift.

6. Advanced Line Profile Studies

6.1. P Cygni Profiles and the Stellar Wind

In the previous section we already alluded to the complexity of some line profiles. We now discuss the behavior of the absorption lines with the highest signal-to-noise ratio, i.e., the Si xiv, Mg xii, and Ne x Ly α transitions (Fig. 11). We observe strong, pure absorption lines with small blueshift (no more than 200 km s^{-1} , Hanke et al. 2008, and paper I), or no shift at all between phases $\phi_{\text{orb}} \sim 0.0$ and ~ 0.2 . Lines at phase $\phi_{\text{orb}} \sim 0.5$ and ~ 0.75 show, however, very different profiles. At phase $\phi_{\text{orb}} \sim 0.5$, we detected *clear* P Cygni line profiles in the spectrum of Cyg X-1. Variable P Cygni-like line profiles have previously been seen, e.g., in Cir X-1 (Schulz & Brandt 2002; Schulz et al. 2008). In Cyg X-1, P Cygni lines have previously been suggested by Schulz et al. (2002) from data from ObsID 107. This 15 ks TE mode observation at phase $\phi_{\text{orb}} = 0.73\text{--}0.76$ was performed during a softer, higher flux state of the source. The observed spectral features were mostly identified with Fe transitions Fe xviii–Fe xxiv, and the authors suggested that absorption and close emission lines could form P Cygni profiles in some cases. They argued, however, that the identification of the Fe lines in the range between 6 and 16 Å is difficult, as many of them are probably blended. Investigating ObsID 2415 at the same orbital phase, Miller et al. (2005) did not find convincing evidence of P Cygni features. Our spectrum of the observation at $\phi_{\text{orb}} \sim 0.75$ (ObsID 3815) does not reveal any P Cygni line pro-

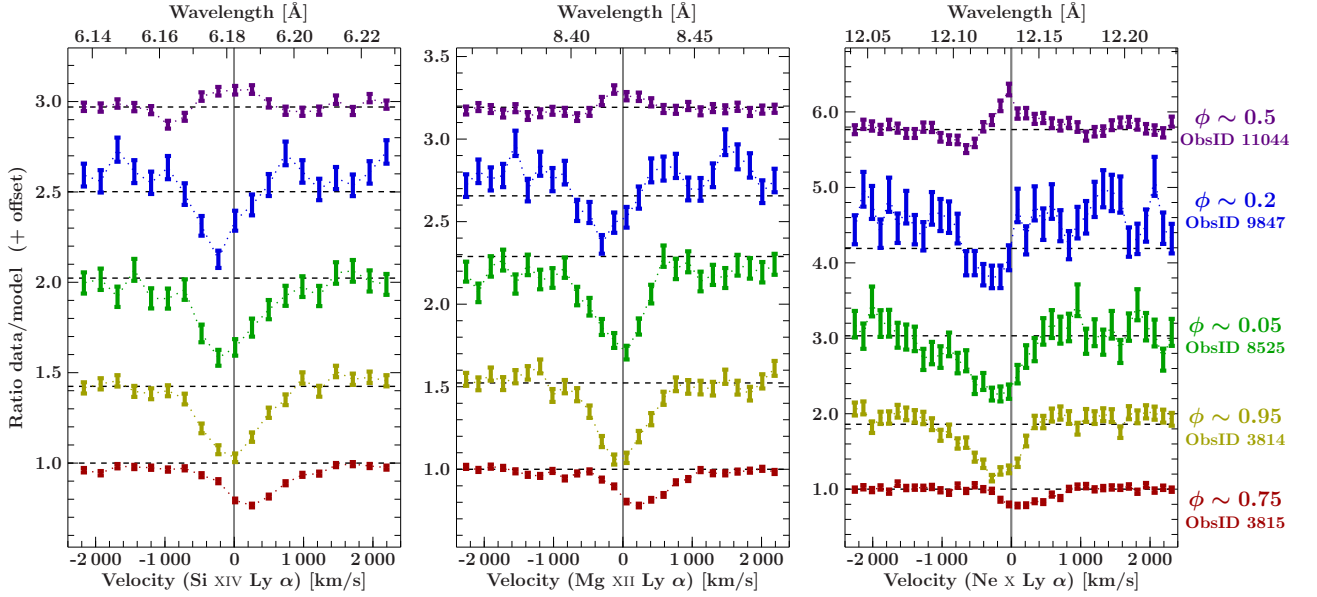


Fig. 11. Line profiles of the three most prominent absorption lines of Si xiv, Mg xii, and Ne x are shown here as they vary over the orbital phase. Lines are displayed as the ratio of data and model, offset for visual clarity. For each line, the vertical grey lines are located at rest wavelengths corresponding to zero velocity shifts. See text for explanation.

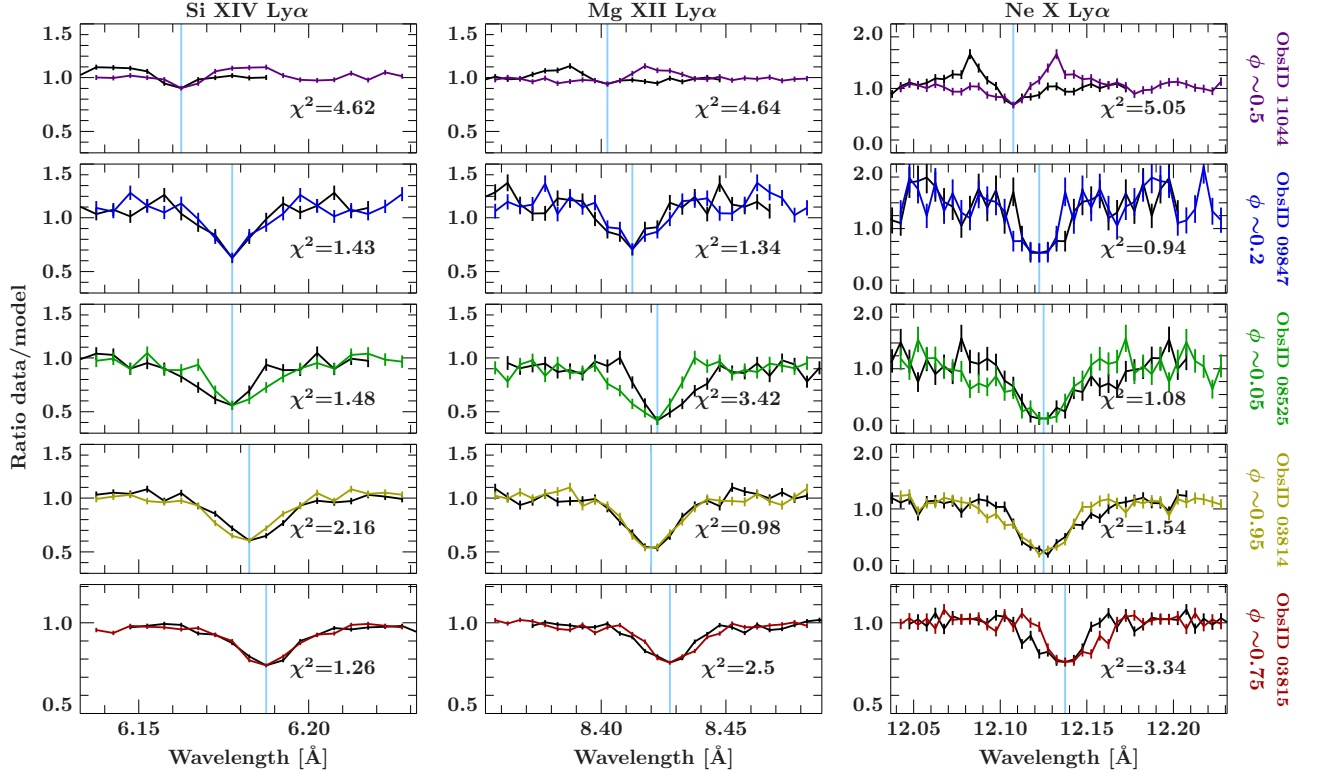


Fig. 12. The same line profiles as in Fig. 11, but this time investigating the symmetry of the profiles. The chosen absorption lines have clear P Cygni profiles at phase $\phi_{\text{orb}} \sim 0.5$. Also other lines show, however, asymmetric profiles. The colored profiles show the original ones, while the black profiles are mirrored at the energy bin with the lowest relative flux value.

files, but we note that the lines appear asymmetric (see Fig. 12 and discussion below).

Given the values from Table A.2, the emission component is much stronger than the absorption. It appears slightly blueshifted, at very low velocities that are – given their uncertainty – still consistent with zero. The blueshift of the weak absorption tails is much higher. Line profiles at phase $\phi_{\text{orb}} \sim 0.75$

are observed as pure absorption lines, but are much weaker than at $\phi_{\text{orb}} \sim 0.0$ and redshifted by 100–400 km s⁻¹. The high blueshift observed in the P Cygni profiles is a direct proof that a non-focused part of the wind also exists on the X-ray irradiated side of the donor star, and that it is accelerated to high velocities. If the different line profiles at $\phi_{\text{orb}} \sim 0.0$ and ~ 0.5 result from the same wind structure, only seen at different viewing angles,

then the weakness of the absorption lines at $\phi_{\text{orb}} \sim 0.5$ confirms that the line of sight at this phase probes less dense regions of the wind than at $\phi_{\text{orb}} \sim 0.0$. Since no net emission is seen at $\phi_{\text{orb}} \sim 0.0$, any emitting gas must be at a small projected velocity, where the emission fills only part of the absorption trough in the continuum radiation created along the line of sight. As this gas is also seen at low velocity from $\phi_{\text{orb}} \sim 0.5$, its full space velocity must be small. It could, e.g., be related to the slow base of the spherical wind, or to the focused wind.

To find possible constraints on the wind in the system, Miller et al. (2005) used the observed lines (Ne ix, Ne x, Si xiii, and Si xiv). Based on calculations by Kallman & McCray (1982) and using the spectral shape and luminosity appropriate for their observations, they find that these absorption features arise in a temperature region spanning over one order of magnitude as $\log T = 4.5\text{--}6.0$. This result already implies that even by investigating the non-dip spectrum only, we probe a multi-temperature region. Based on the ionization parameter and simplifying geometry assumptions, Miller et al. determined the distance of the absorbing region from the ionizing source to be $\sim 3 \times 10^{11} - 10^{12}$ cm.

Most of the line profiles shown in Fig. 11 give an impression of asymmetry. To describe it quantitatively, we first mirrored the measured line profile at the energy bin with the lowest relative flux value of the data/model ratio (Fig. 12). The original and the flipped profiles were then treated as “data” and “model” and a χ^2 -type value was calculated to describe the “goodness” of the overlap according to

$$\chi^2 = \frac{1}{N} \sum \frac{(y_{\text{original}} - y_{\text{flipped}})^2}{\sigma_{\text{original}}^2 + \sigma_{\text{flipped}}^2} \quad (4)$$

where N is the total number of bins which were taken into account to calculate the χ^2 . Both profiles and obtained values of χ^2 are shown in Fig. 12. The highest χ^2 values were obtained for the P Cygni profiles in ObsID 11044. Mg xii in ObsID 8525 and Ne x in ObsID 3815 would be also described as asymmetric, but for the latter this might also be caused by blending with Fe lines. Setting a threshold of $\chi^2 = 1.5$, all lines in ObsID 9847, Si xiv and Ne x in ObsID 8525, Mg xii in ObsID 3814 and Si xiv in ObsID 3815 would be considered symmetric. For Ne x in ObsIDs 9847 and 8525, the data have, however, high uncertainties, and are therefore not very sensitive to detecting asymmetry.

6.2. Properties of the X-ray emitting gas: density diagnostics of the Mg xi He-like triplet

Due to the P Cygni profiles, the location of the absorber in ObsID 11044 is difficult to constrain. This observation, however, contains a strong He-like Mg triplet, i.e., the forbidden, intercombination, and recombination lines f, i, and r, between 9.1 and 9.4 Å which is suitable for plasma diagnostics (Fig. A.4). The existence of these lines allows us to determine the physical condition of the location of the emitter, although the absorber location is indeterminable. With the triplet lines all being seen in emission, their intensity ratios $G(T_e) = (i + f)/r$ and $R(n_e) = f/i$ can be used to directly estimate electron temperature and density of the emitting plasma (Gabriel & Jordan 1969; Porquet & Dubau 2000). Note that in ObsID 3814, $\phi_{\text{orb}} \sim 0.0$, which we studied in paper I, only Mg xi i and f are seen in emission, while Mg xi r is in absorption, allowing only for the R -ratio to be analyzed.

In ObsID 11044, $G = 1.6 \pm 0.5 \ll 4$ indicates a hybrid plasma where next to photoionization, collisional ionization plays an important role as well (Porquet & Dubau 2000). The G value

corresponds to an electron temperature of roughly $(3\text{--}5) \times 10^6$ K, depending on the ratio of H-like to He-like ions. Since G is a rather steep function of temperature in that range, the uncertainty of G has only very little effect on the temperature. Note that the P Cygni profile of the resonance line also adds an uncertainty to its intensity, and therefore, G .

The R -ratio of 0.6 ± 0.5 corresponds to an electron density of $\sim 4 \times 10^{13} \text{ cm}^{-3}$. The presence of the strong UV field produced by HDE 226868 can, however, deplete the metastable upper level of the forbidden line by photoexcitation, lowering the measured R -ratio (Mewe & Schrijver 1978; Kahn et al. 2001). Thus, the derived density constitutes an upper limit.

Similar results can be obtained by directly fitting the He-like triplet using results from collisional plasma calculations by D. Huenemoerder (priv. comm., see <http://space.mit.edu/cxc/analysis/hemodifier/index.html>), which however, does not take the effects of UV radiation into account either. This fit gives $T_e \sim 3 \times 10^6$ K and $n_e \sim 6 \times 10^{13} \text{ cm}^{-3}$.

In ObsID 3814 we could resolve two sets of Mg xi i and f lines, one unshifted and the other one redshifted (paper I). Within their uncertainties, the plasma seen in ObsID 11044 shows the same R -ratio, i.e., the same electron density, as the redshifted Mg triplet in ObsID 3814.

We note that the density determined from the emission lines is a factor of ~ 1000 higher than the density of the region where the absorption is thought to occur. This could mean that the emission component could originate in emitting high density regions, such as clouds, that are mixed into the absorber. Alternatively, the high density could point at an origin not in the wind but in the denser regions of the accretion flow within the Bondi radius.

7. Summary

Stellar winds of massive stars are highly inhomogeneous phenomena: they show temperatures spanning several orders of magnitude, turbulent velocities, and highly variable densities. Gratings of the *Chandra* observatory provide us with the first real opportunity to investigate the narrow spectral lines of the stellar winds in great detail and so allow us to probe this variable environment. Cyg X-1 as a nearby, bright, and persistent source is an ideal target for such a study. In this work, we presented the most extensive analysis of the *Chandra*-HETGS hard state spectra of Cyg X-1 so far. We investigated five spectra that cover the most important segments of orbital phase: stellar wind in its focused stream at $\phi_{\text{orb}} \sim 0.0$, the opposite site of the focused wind at $\phi_{\text{orb}} \sim 0.5$, as well as at parts perpendicular to the binary axis at $\phi_{\text{orb}} \sim 0.2$ and ~ 0.75 . This is the second paper in the series; paper I presented analysis of one of the observations (ObsID 3814, $\phi_{\text{orb}} \sim 0.95$), focusing only on spectra extracted at the constant flux level (dips excluded). Here, we analyzed the non-dip spectra of the remaining observations, and discussed their variation over the orbital phase.

The most important results of our analysis are:

1. The intensity of dipping in light curves is phase dependent. Strong dips are observed along the binary axis at $\phi_{\text{orb}} \sim 0.0$ while the light curve outside the focused stellar wind at $\phi_{\text{orb}} \sim 0.5$ is free of absorption dips in these observations.
2. Non-dip spectra reveal absorption lines of H- and He-like ions of S, Si, Al, Mg, Na, and Ne as well as L-shell Fe transitions corresponding to highly ionized material. Spectra measured close to $\phi_{\text{orb}} \sim 0.0$ also show lines of lower ionized stages of Si xii–Si ix. The spectrum observed outside of the wind at $\phi_{\text{orb}} \sim 0.5$ shows clear P Cygni profiles.

3. The neutral Ne K absorption edge was prominent in all investigated spectra, such that we were able to measure the neutral Ne column density independently from total column. The values vary moderately within $N_{\text{Ne}} = (0.5\text{--}1.5) \times 10^{18} \text{ cm}^{-2}$, attaining lowest values outside of the wind at $\phi_{\text{orb}} \sim 0.5$, and highest values at $\phi_{\text{orb}} \sim 0.2$. The Fe absorption edge was only resolved in the spectrum at $\phi_{\text{orb}} \sim 0.5$, giving $N_{\text{Fe}} = 0.15 \pm 0.02 \times 10^{18} \text{ cm}^{-2}$. Deriving N_{H} values from continuum fitting to the gratings data suffers from a large systematic error and yields values that are strongly biased towards lower columns.
4. Column densities obtained from the analysis of the ionized absorption lines are phase dependent, and therefore intrinsic to the source. They are highest around $\phi_{\text{orb}} \sim 0.0$, i.e., in the focused wind stream, and imply that the observed medium is almost fully ionized. The observed elements appear to be overabundant with respect to solar abundances.
5. Doppler shifts, $\pm 500 \text{ km s}^{-1}$, vary strongly with orbital phase. Both, the column of the absorber and the Doppler shift are consistent with an absorber location that is less than $0.5d$ away from the black hole, where d is the distance between the donor star and the black hole. The observations suggest that we observe a complex ionization structure.
6. The spectrum at $\phi_{\text{orb}} \sim 0.5$ shows the Mg He-triplet suitable for plasma diagnostics, suggesting that we also see a plasma with an electron temperature of $(3\text{--}5) \times 10^6 \text{ K}$ which is much denser than the locations in the wind responsible for absorption, e.g., clumps in the stellar wind.

In the next paper of this series we will be studying the properties of the gas responsible for the absorption dips in the light curves.

Acknowledgements. The research leading to these results was funded by the European Community's Seventh Framework Programme (FP7/2007-2013) under grant agreement number ITN 215212 "Black Hole Universe" and by the Bundesministerium für Wirtschaft und Technologie under grant numbers DLR 50OR 0701 and 50OR 1113. This work was partially completed by Lawrence Livermore National Laboratory (LLNL) under Contract DE-AC52-07NA27344, and is supported by NASA grants to LLNL. Support for this work was also provided by NASA through the Smithsonian Astrophysical Observatory (SAO) contract SV3-73016 to MIT for Support of the Chandra X-Ray Center (CXC) and Science Instruments; CXC is operated by SAO for and on behalf of NASA under contract NAS8-03060. We acknowledge the support by the DFG Cluster of Excellence "Origin and Structure of the Universe" and are grateful for the support by MCB through the Computational Center for Particles and Astrophysics (C2PAP). We are thankful to John E. Davis for the SLXfig package that was used to create the figures throughout this paper, to David Huenemoerder for the AGLC routine handling the grating lightcurves and routines related to plasma diagnostics, and to Thomas Dauser for parallel computing routines. This research has made use of the MAXI data provided by RIKEN, JAXA, and the MAXI team.

References

Bałucińska-Church, M., Belloni, T., Church, M. J., & Hasinger, G. 1995, *A&A*, 302, L5
Bałucińska-Church, M., Church, M. J., Charles, P. A., et al. 2000, *MNRAS*, 311, 861
Behar, E. & Netzer, H. 2002, *ApJ*, 570, 165
Belloni, T. 2004, *Nucl. Phys. B Proc. Suppl.* 132, 337
Belloni, T. M. 2010, in *The Jet Paradigm – From Microquasars to Quasars*, ed. T. M. Belloni, *Lecture Notes in Physics* 794 (Berlin, Springer), 53
Blondin, J. M. 1994, *ApJ*, 435, 756
Blondin, J. M., Stevens, I. R., & Kallman, T. R. 1991, *ApJ*, 371, 684
Blondin, J. M. & Woo, J. W. 1995, *ApJ*, 445, 889
Bondi, H. & Hoyle, F. 1944, *MNRAS*, 104, 273
Boroson, B. & Vrtilek, S. D. 2010, *ApJ*, 710, 197
Bowyer, S., Byram, E. T., Chubb, T. A., & Friedman, H. 1965, *Ann. Astrophys.*, 28, 791
Brocksopp, C., Fender, R. P., Larionov, V., et al. 1999, *MNRAS*, 309, 1063
Caballero-Nieves, S. M., Gies, D. R., Bolton, C. T., et al. 2009, *ApJ*, 701, 1895

Canizares, C. R., Davis, J. E., Dewey, D., et al. 2005, *PASP*, 117, 1144
Castor, J. I., Abbott, D. C., & Klein, R. I. 1975, *ApJ*, 195, 157
Duro, R., Dauser, T., & Grinberg, V., et al. 2016, *A&A*, in press (arXiv:1602.08756)
Duro, R., Dauser, T., Wilms, J., et al. 2011, *A&A*, 533, L3
Fabian, A. C., Wilkins, D. R., Miller, J. M., et al. 2012, *MNRAS*, 424, 217
Feldmeier, A., Puls, J., & Pauldrach, A. W. A. 1997, *A&A*, 322, 878
Fender, R., Corbel, S., Tzioumis, T., et al. 1999, *ApJ*, 519, L165
Feng, Y. X. & Cui, W. 2002, *ApJ*, 564, 953
Foster, A. R., Ji, L., Smith, R. K., & Brickhouse, N. S. 2012, *ApJ*, 756, 128
Friend, D. B. & Castor, J. I. 1982, *ApJ*, 261, 293
Gabriel, A. H. & Jordan, C. 1969, *MNRAS*, 145, 241
Garmire, G. P., Bautz, M. W., Ford, P. G., Nousek, J. A., & Ricker, Jr., G. R. 2003, in *X-Ray and Gamma-Ray Telescopes and Instruments for Astronomy*, ed. J. E. Trümper & H. D. Tananbaum, *Proc. SPIE* 4851 (Bellingham, SPIE), 28–44
Gierliński, M., Zdziarski, A. A., Poutanen, J., et al. 1999, *MNRAS*, 309, 496
Gies, D. R. & Bolton, C. T. 1986, *ApJ*, 304, 389
Gies, D. R., Bolton, C. T., Blake, R. M., et al. 2008, *ApJ*, 678, 1237
Gies, D. R., Bolton, C. T., Thomson, J. R., et al. 2003, *ApJ*, 583, 424
Grinberg, V., Hell, N., Pottschmidt, K., et al. 2013, *A&A*, 554, A88
Grinberg, V., Leutenegger, M. A., Hell, N., et al. 2015, *A&A*, 576, A117
Hanke, M. 2011, *Dissertation*, Friedrich-Alexander-Universität Erlangen-Nürnberg, Erlangen
Hanke, M., Wilms, J., Nowak, M. A., Barragán, L., & Schulz, N. S. 2010, *A&A*, 509, L8
Hanke, M., Wilms, J., Nowak, M. A., et al. 2009, *ApJ*, 690, 330
Hanke, M., Wilms, J., Nowak, M. A., et al. 2008, *PoS, MQW7*, 29
Hell, N., Miškovičová, I., Brown, G. V., et al. 2013, *Phys. Scr.*, T156, 014008
Herrero, A., Kudritzki, R. P., Gabler, R., Vilchez, J. M., & Gabler, A. 1995, *A&A*, 297, 556
Holt, S. S., Boldt, E. A., Serlemitsos, P. J., & Kaluzienski, L. J. 1976, *ApJ*, 203, L63
Houck, J. C. & Denicola, L. A. 2000, in *Astronomical Data Analysis Software and Systems IX*, ed. N. Manset, C. Veillet, & D. Crabtree, *Astron. Soc. Pacific Conf. Ser.* 216, 591
Jahoda, K., Markwardt, C. B., Radeva, Y., et al. 2006, *ApJS*, 163, 401
Juett, A. M., Wilms, J., Schulz, N. S., & Nowak, M. A. 2006, *Bull. AAS*, 38, 921
Kahn, S. M., Leutenegger, M. A., Cottam, J., et al. 2001, *A&A*, 365, L312
Kallman, T. R. & McCray, R. 1982, *ApJS*, 50, 263
Kitamoto, S., Egoshi, W., Miyamoto, S., et al. 2000, *ApJ*, 531, 546
Kitamoto, S., Miyamoto, S., Tanaka, Y., et al. 1984, *PASJ*, 36, 731
Kitamoto, S., Miyamoto, S., & Yamamoto, T. 1989, *PASJ*, 41, 81
Lachowicz, P., Zdziarski, A. A., Schwarzenberg-Czerny, A., Pooley, G. G., & Kitamoto, S. 2006, *MNRAS*, 368, 1025
Lampton, M., Margon, B., & Bowyer, S. 1976, *ApJ*, 208, 177
Levine, A. M., Bradt, H., Cui, W., et al. 1996, *ApJ*, 469, L33
Li, F. K. & Clark, G. W. 1974, *ApJ*, 191, L27
Manousakis, A. 2011, *Thèse de doctorat*, Université de Genève, Geneva
Marshall, H. L., Schulz, N. S., Fang, T., et al. 2001, in *Proc. X-ray Emission from Accretion onto Black Holes*, ed. T. Yaqoob & J. H. Krolik, (astro-ph/0111464)
Mason, K. O., Hawkins, F. J., Sanford, P. W., Murdin, P., & Savage, A. 1974, *ApJ*, 192, L65
Matsuoka, M., Kawasaki, K., Ueno, S., et al. 2009, *PASJ*, 61, 999
Mewe, R. & Schrijver, J. 1978, *A&A*, 65, 99
Mihalas, D. 1978, *Stellar Atmospheres*, 2nd edn. (San Francisco, W.H. Freeman and Co.)
Miller, J. M., Fabian, A. C., Wijnands, R., et al. 2002, *ApJ*, 578, 348
Miller, J. M., Wojdowski, P., Schulz, N. S., et al. 2005, *ApJ*, 620, 398
Mujeres, L. E., Vink, J. S., de Koter, A., Müller, P. E., & Langer, N. 2012, *A&A*, 537, A37
Nowak, M. A., Hanke, M., Trowbridge, S. N., et al. 2011, *ApJ*, 728, 13
Orosz, J. A., McClintock, J. E., Aufdenberg, J. P., et al. 2011, *ApJ*, 742, 84
Oskinova, L. M., Feldmeier, A., & Kretschmar, P. 2012, *MNRAS*, 421, 2820
Parsignault, D. R., Grindlay, J. E., Schnopper, H. W., Schreier, E. J., & Gursky, H. 1976, in *X-ray binaries*, ed. Y. Kondo & E. Boldt, *NASA SP-389*, 429–442
Porquet, D. & Dubau, J. 2000, *A&AS*, 143, 495
Pottschmidt, K., Wilms, J., Nowak, M. A., et al. 2003, *A&A*, 407, 1039
Poutanen, J., Zdziarski, A. A., & Ibragimov, A. 2008, *MNRAS*, 389, 1427
Pravdo, S. H., White, N. E., Becker, R. H., et al. 1980, *ApJ*, 237, L71
Priedhorsky, W., Garmire, G. P., Rothschild, R., et al. 1979, *ApJ*, 233, 350
Rahoui, F., Lee, J. C., Heinz, S., et al. 2011, *ApJ*, 736, 63
Reid, M. J., McClintock, J. E., Narayan, R., et al. 2011, *ApJ*, 742, 83
Remillard, R. A. & Canizares, C. R. 1984, *ApJ*, 278, 761
Sako, M., Liedahl, D. A., Kahn, S. M., & Paerels, F. 1999, *ApJ*, 525, 921
Schulz, N. S. & Brandt, W. N. 2002, *ApJ*, 572, 971
Schulz, N. S., Cui, W., Canizares, C. R., et al. 2002, *ApJ*, 565, 1141

- Schulz, N. S., Kallman, T. E., Galloway, D. K., & Brandt, W. N. 2008, *ApJ*, 672, 1091
- Shaposhnikov, N., Jahoda, K., Markwardt, C., Swank, J., & Strohmayer, T. 2012, *ApJ*, 757, 159
- Sundqvist, J. O. & Owocki, S. P. 2013, *MNRAS*, 428, 1837
- Tarter, C. B., Tucker, W. H., & Salpeter, E. E. 1969, *ApJ*, 156, 943
- Tomsick, J. A., Nowak, M. A., Parker, M., et al. 2014, *ApJ*, 780, 78
- Verner, D. A., Ferland, G. J., Korista, K. T., & Yakovlev, D. G. 1996, *ApJ*, 465, 487
- Vrtilek, S. D. & Boroson, B. S. 2013, *MNRAS*, 428, 3693
- Vrtilek, S. D., Boroson, B. S., Hunacek, A., Gies, D., & Bolton, C. T. 2008, *ApJ*, 678, 1248
- Walborn, N. R. 1973, *ApJ*, 179, L123
- Webster, B. L. & Murdin, P. 1972, *Nat*, 235, 37
- Wen, L., Cui, W., Levine, A. M., & Bradt, H. V. 1999, *ApJ*, 525, 968
- Wilms, J., Allen, A., & McCray, R. 2000, *ApJ*, 542, 914
- Wilms, J., Nowak, M. A., Pottschmidt, K., Pooley, G. G., & Fritz, S. 2006, *A&A*, 447, 245
- Xiang, J., Lee, J. C., Nowak, M. A., & Wilms, J. 2011, *ApJ*, 738, 78

Appendix A: Line Series Parameters & Spectra

Table A.1. H-like, He-like and Fe absorption lines at $\phi_{\text{orb}} \sim 0.75$, $\phi_{\text{orb}} \sim 0.05$, and ~ 0.2 (ObsID 3815, 8525, and 9847)

	ObsID 3815 $\phi_{\text{orb}} \sim 0.75$			ObsID 8525 $\phi_{\text{orb}} \sim 0.05$			ObsID 9847 $\phi_{\text{orb}} \sim 0.2$		
	Column density N_i [10^{16} cm^{-2}]	Velocity shift Δv [km s^{-1}]	Thermal broadening ξ [km s^{-1}]	Column density N_i [10^{16} cm^{-2}]	Velocity shift Δv [km s^{-1}]	Thermal broadening ξ [km s^{-1}]	Column density N_i [10^{16} cm^{-2}]	Velocity shift Δv [km s^{-1}]	Thermal broadening ξ [km s^{-1}]
H-like lines									
Ne x	$1.76^{+0.16}_{-0.13}$	190^{+27}_{-22}	240 ± 50	160^{+130}_{-70}	-130^{+70}_{-60}	73^{+20}_{-18}	160^{+80}_{-60}	-360 ± 40	69^{+16}_{-12}
Na xi	$1.94^{+0.18}_{-0.17}$	350^{+100}_{-90}	1120^{+140}_{-120}	$7.3^{+1.7}_{-1.6}$	0.0^{+320}_{-260}	1400^{+600}_{-400}	$6.9^{+1.3}_{-0.9}$	240^{+360}_{-220}	1910^{+300}_{-270}
Mg xii	3.24 ± 0.15	311^{+20}_{-18}	328^{+160}_{-250}	$8.1^{+1.6}_{-1.8}$	-80 ± 70	370^{+130}_{-100}	$6.1^{+1.0}_{-1.3}$	-200 ± 90	420^{+90}_{-250}
Al xiii	$0.61^{+0.14}_{-0.13}$	130 ± 100	360^{+240}_{-180}	≤ 7.9	0.0 ± 10^4	$\leq 3 \times 10^4$	≤ 8.2	$(-0.06^{+1.05}_{-0.20}) \times 10^4$	≤ 8540
Si xiv	$4.44^{+0.20}_{-0.19}$	259^{+27}_{-80}	420 ± 50	$300^{+100}_{-85.2}$	-90 ± 50	≤ 517	6.7^{+271}_{-40}	$-180^{+100}_{-120.51}$	$200^{+200}_{-2.8}$
S xvi	3.4 ± 0.5	230^{+80}_{-70}	220 ± 170	$6.1^{+1.2}_{-2.2}$	-100 ± 400	320^{+490}_{-280}	60^{+40}_{-50}	$-323.64^{+0.24}_{-120.51}$	≤ 2.8
Ar xviii	—	—	—	5 ± 4	$(-1.00^{+0.08}_{-0.00}) \times 10^4$	1400^{+1900}_{-1200}	≤ 26	$(0.1 \pm 1.0) \times 10^4$	≤ 1875
Ca xix	—	—	—	14^{+76}_{-13}	-400^{+600}_{-1000}	≤ 2586	≤ 60	$\leq 10^4$	≤ 6800
He-like lines									
Ne ix	0.89 ± 0.13	390^{+100}_{-90}	650^{+140}_{-100}	19^{+12}_{-120}	150^{+90}_{-120}	120^{+140}_{-50}	$10.5^{+2.8}_{-3.3}$	-250^{+130}_{-150}	410^{+120}_{-100}
Na x	0.99 ± 0.09	870^{+70}_{-60}	830^{+80}_{-80}	$6.0^{+138.5}_{-2.8}$	-300 ± 100	≤ 130	$50^{+3.3}_{-25}$	220 ± 60	$8.9^{+6.6}_{-2.8}$
Mg xi	0.68 ± 0.08	370^{+60}_{-50}	350^{+90}_{-90}	11^{+6}_{-4}	-160^{+80}_{-70}	84^{+37}_{-25}	10^{+8}_{-4}	-200^{+80}_{-70}	76^{+24}_{-24}
Al xii	$0.22^{+0.06}_{-0.07}$	240^{+120}_{-100}	270^{+190}_{-260}	$7.2^{+2.2}_{-2.3}$	$(1.00^{+0.00}_{-0.26}) \times 10^4$	$(2.3^{+0.7}_{-0.6}) \times 10^4$	7^{+8}_{-6}	-150^{+80}_{-160}	11^{+17}_{-10}
Si xiii	$4.4^{+1.0}_{-1.2}$	317^{+1}_{-40}	16^{+7}_{-5}	14^{+14}_{-7}	-210^{+90}_{-50}	93^{+33}_{-25}	≤ 90	-310^{+150}_{-80}	220^{+95}_{-23}
S xv	$1.37^{+0.22}_{-0.20}$	230^{+80}_{-70}	310 ± 150	4.2 ± 1.5	300 ± 400	900 ± 600	≤ 37	-30^{+63}_{-160}	16^{+63}_{-6}
Ar xvii	≤ 0.5	$(0.04^{+0.96}_{-0.20}) \times 10^4$	$(2.25^{+0.75}_{-0.04}) \times 10^4$	—	—	—	$3.7297^{+0.0004}_{-2.4044}$	$(0.766^{+0.001}_{-0.008}) \times 10^4$	$36.968^{+0.004}_{-27.427}$
Ca xix	—	—	—	—	—	—	≤ 8	$\leq 10^4$	4300^{+2700}_{-3500}
Fe lines									
Fe xvii	—	—	—	3^{+73}_{-1}	-260^{+140}_{-130}	130^{+120}_{-100}	3^{+23}_{-1}	-230^{+90}_{-80}	80^{+90}_{-70}
Fe xviii	1.47 ± 0.16	144^{+28}_{-18}	34^{+7}_{-3}	$4.2^{+1.5}_{-1.3}$	-210^{+160}_{-120}	100^{+130}_{-50}	$3.3^{+1.7}_{-1.0}$	-410^{+130}_{-140}	100^{+100}_{-60}
Fe xix	$2.96^{+0.29}_{-0.73}$	225.2 ± 0.2	$19.06^{+0.89}_{-0.07}$	$6.7^{+1.3}_{-1.3}$	-390^{+100}_{-90}	150^{+130}_{-90}	$2.3^{+0.9}_{-0.7}$	-220^{+160}_{-200}	130^{+310}_{-80}
Fe xx	$1.64^{+0.10}_{-0.06}$	60 ± 40	400^{+40}_{-80}	$4.6^{+1.8}_{-0.9}$	-130^{+190}_{-250}	350^{+370}_{-280}	$3.8^{+0.7}_{-1.0}$	-330^{+130}_{-130}	200^{+260}_{-150}
Fe xxi	$1.16^{+0.08}_{-0.08}$	240 ± 50	740^{+70}_{-70}	$2.7^{+0.9}_{-0.8}$	-310^{+200}_{-200}	420^{+380}_{-300}	1.6 ± 0.4	-440^{+220}_{-220}	220^{+280}_{-50}
Fe xxii	$2.39^{+0.38}_{-0.28}$	182 ± 10	21 ± 3	$2.6^{+1.8}_{-0.8}$	100^{+190}_{-250}	230^{+350}_{-100}	$7.3^{+3.0}_{-4.9}$	-158^{+11}_{-3}	12^{+32}_{-6}
Fe xxiii	$6.2^{+1.0}_{-0.6}$	231^{+10}_{-9}	$8.4^{+3.4}_{-1.6}$	≤ 34	200^{+500}_{-1000}	≤ 864	$\leq 1.6 \times 10^{-3}$	$(0.0 \pm 1.0) \times 10^4$	$\leq 1.27 \times 10^4$
Fe xxiv	$2.21^{+0.18}_{-0.13}$	261^{+25}_{-15}	250 ± 50	70^{+100}_{-70}	-114^{+26}_{-64}	10^{+10}_{-6}	4.5 ± 1.0	10 ± 60	440^{+230}_{-190}

Notes. ^(†) Unconstrained parameter. The calculation has reached one or both limits of the range set for this parameter. Note that primarily affected line series are those consisting of weak or possibly blended lines of Al, Ar, Ca or Fe.

Table A.2. Parameters for spectral line features for ObsID 11044. All lines, including the emission and absorption line portion of the P Cygni line profiles, are modeled with Voigt profiles.

P Cygni profiles												
Line	Absorption				Emission							
	Reference wavelength λ_{theory} (Å)	Obs. wavel. λ_{obs} (Å)	Norm A ($10^{-3} \text{ ph s}^{-1} \text{ cm}^{-2}$)	Thermal broadening v_{therm} (km s^{-1})	FWHM Γ (keV)	Velocity shift Δv (km s^{-1})	Column density N_i (10^{16} cm^{-2})	Obs. wavel. λ_{obs} (Å)	Norm A ($10^{-3} \text{ ph s}^{-1} \text{ cm}^{-2}$)	Thermal broadening v_{therm} (km s^{-1})	FWHM Γ (keV)	Velocity shift Δv (km s^{-1})
Si xiv Ly α	6.1805	6.166(2)	-0.12 ± 0.05	90^{+200}_{-80}	–	-700 ± 100	0.9(3)	6.181(3)	0.21 ± 0.06	310^{+200}_{-230}	–	20 ± 150
Mg xii Ly α	8.4192	8.402(4)	-0.13 ± 0.07	≤ 200	≤ 0.010	-610 ± 140	0.7(2)	8.419(3)	$0.17^{+0.07}_{-0.05}$	270^{+230}_{-190}	–	-10 ± 110
Nex Ly α	12.1317	12.115(3)	$-0.7^{+0.2}_{-0.1}$	500^{+140}_{-340}	≤ 0.012	-410 ± 70	3.0(4)	12.128(2)	$0.97^{+0.35}_{-0.28}$	≤ 269	$0.009^{+0.005}_{-0.008}$	-90 ± 50
Nex Ly β	10.2327	10.231(2)	$-4.2^{+2.6}_{-0.32}$	700^{+800}_{-1000}	$0.04^{+0.01}_{-0.03}$	-50 ± 60	74(2)	10.237(2)	$4.8^{+2.4}_{-0.36}$	≤ 1082	$0.056^{+0.014}_{-0.037}$	130 ± 60
Nex Ly δ	9.4794	9.464(1)	$-0.56^{+0.22}_{-0.38}$	2000^{+1900}_{-1600}	≤ 0.05	-490 ± 30	83(19)	9.500(6)	$0.27^{+0.36}_{-0.16}$	≤ 821	≤ 0.05	650 ± 190
Mg xi triplet												
Mg xir	9.1687	9.14(1)	-0.3 ± 0.1	≤ 200	$0.05^{+0.00}_{-0.02}$	-940 ± 330	0.9(4)	9.168(2)	$0.26^{+0.06}_{-0.07}$	280 ± 100	≤ 0.008	-20 ± 70
Mg xii	9.2312							9.228(5)	$0.22^{+0.16}_{-0.09}$	≤ 700	≤ 0.026	-100 ± 160
Mg xif	9.3143							9.308(7)	$0.16^{+0.09}_{-0.09}$	≤ 810	≤ 0.025	-200 ± 230
Emission lines												
Fe K α	1.9373							1.937(3)	1.0 ± 0.4	≤ 950	≤ 0.5	-50 ± 450
Fe xxv	1.8504							1.862(6)	0.22 ± 0.2	≤ 970	≤ 0.5	1880 ± 970
Si xiii He f	6.7403							6.741(1)	0.28 ± 0.07	≤ 240	≤ 0.017	30 ± 40
Ne ix He i	13.55							13.55(2)	0.28 ± 0.12	600 ± 400	–	0 ± 440
Absorption lines												
Si xii (Li)	6.7176	6.705(1)	-0.13 ± 0.04	26^{+27}_{-8}	–	-670 ± 50	0.6(2)					
Fe xxi	12.2840	12.265(7)	-0.15 ± 0.06	170^{+180}_{-160}	–	-460 ± 170	–					

Notes. Number in brackets corresponds to the uncertainty in units of the last digit. Equivalent width and column density are not calculated for emission lines.

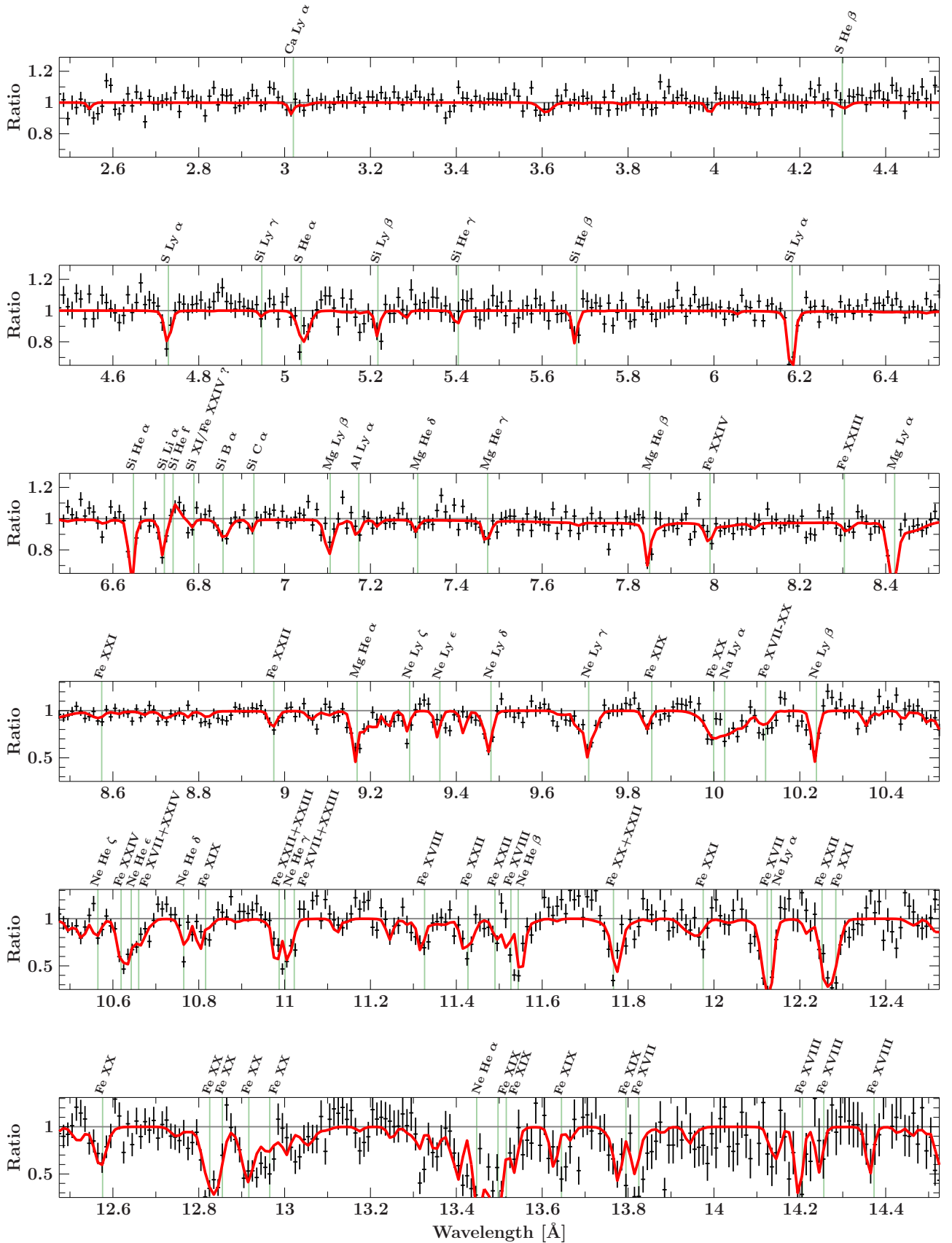


Fig. A.1. Non-dip spectrum of ObsID 8525 – displayed as the ratio between data and absorbed power-law continuum model – showing the absorption lines observed in the spectrum. Due to a relatively short exposure time of only 4.4 ks, the HEG spectra are worse than MEG at longer wavelengths. Data from HEG were therefore scaled to MEG data for visual reasons. The red line shows lines modeled with line series. Each of them is labeled at its rest wavelength. There are no significant emission lines in the spectrum except the Si XIII forbidden line. Instead, absorption lines from Si XII (Li-like), possibly Si XI (Be-like), Si X (B-like), and Si IX (C-like), although quite weak, can be clearly identified in the “Si region” between 6.6 Å and 7 Å.

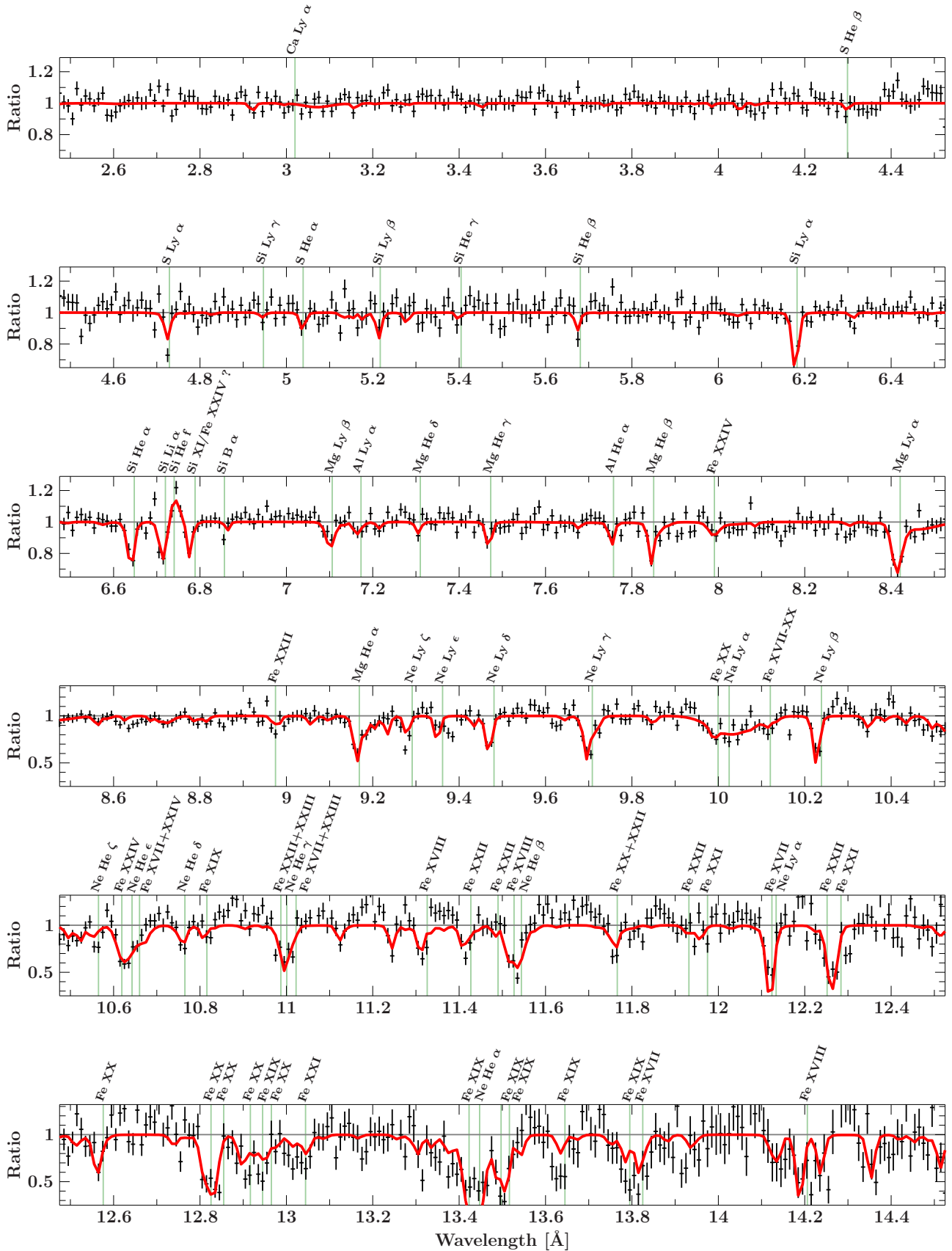


Fig. A.2. Line identifications for ObsID 9847. Non-dip data displayed as ratio between data and absorbed power-law continuum model.

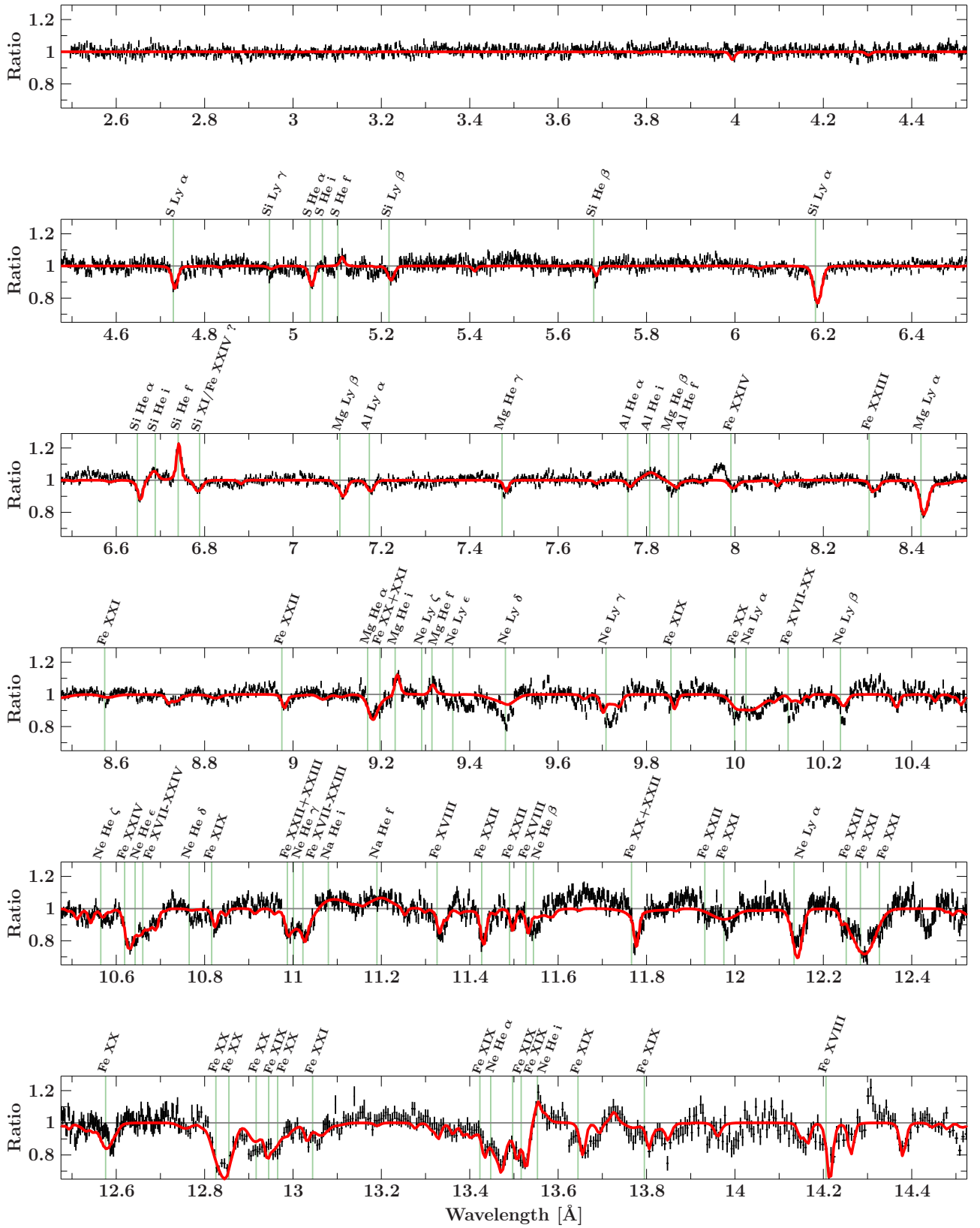


Fig. A.3. Non-dip spectrum of ObsID 3815 – displayed as the ratio between data and absorbed power-law continuum model – showing the H- and He-like absorption lines, as well as the i and f emission lines of the hot gas of the stellar wind. The spectra of HEG±1 and MEG±1 were combined and binned to the same signal-to-noise ratio ($S/N = 10$) as for fitting. Especially notable are lines of $Ne\ x\beta$ at 10.24 Å, $Ne\ x\gamma$ at 9.71 Å and $Ne\ x\delta$ at 9.48 Å, because they are much stronger in the data than the profiles that are predicted by the model. We did not manage to identify the emission feature at ~ 7.98 Å. It is visible also in ObsID 1044 (Fig. A.4), but not in ObsIDs 8525 and 9847 (Figs. A.1 and A.2).

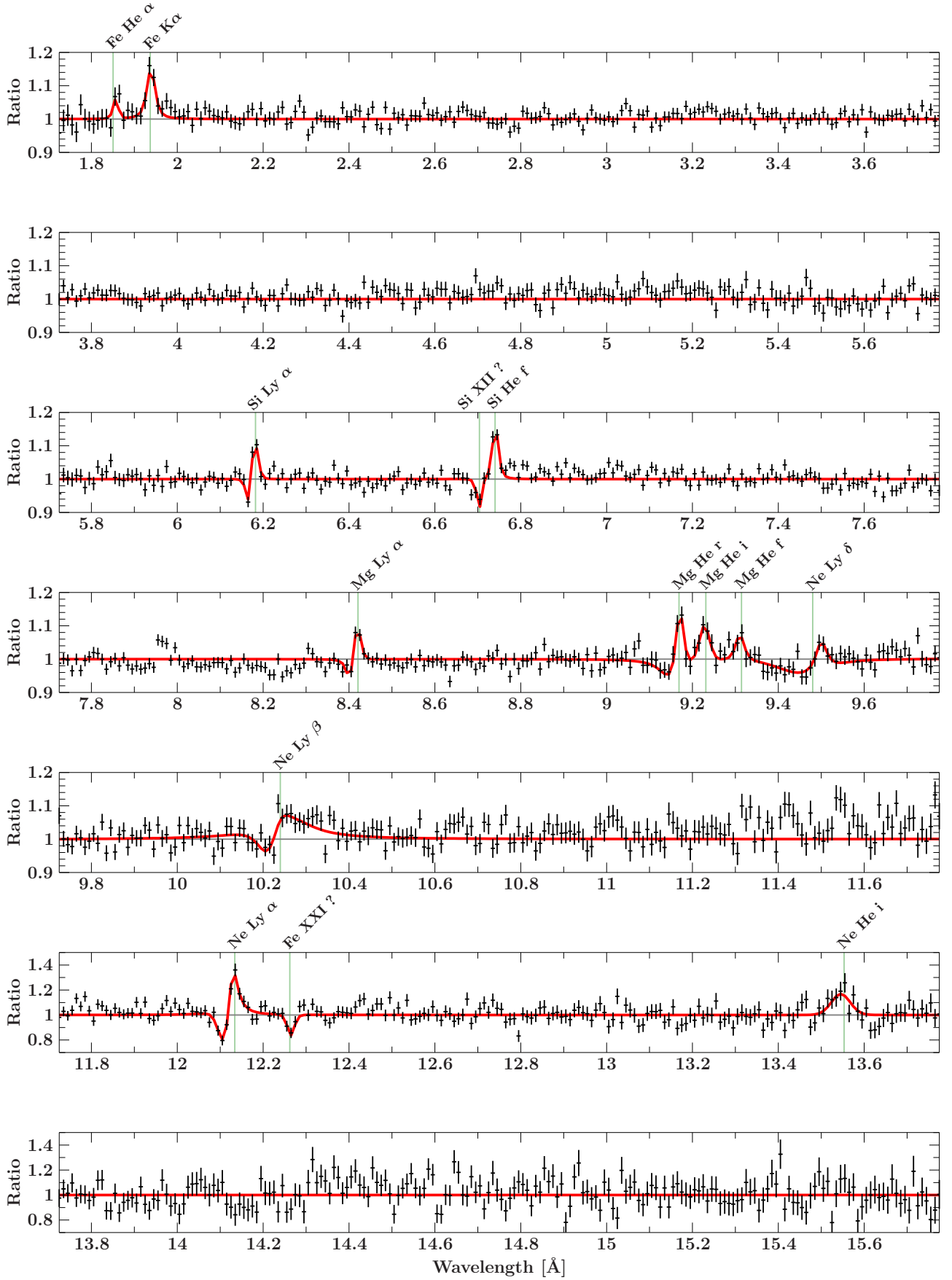


Fig. A.4. Spectrum of ObsID 11044 displayed as the ratio between data and absorbed power-law continuum model. The most prominent absorption and emission lines have been fitted with Voigt profiles. The Ly α lines of H-like Si, Mg, and Ne show clear P Cygni profiles. The absorption line at 6.70 Å, however, cannot be related to the emission line at 6.74 Å, if the latter is due to the (dipole-) forbidden transition of Si XII.

Appendix B: Diffraction Order Determination in CIAO Data Reduction

A data processing problem that would have strongly affected any further analysis consists in the incorrect determination of the diffraction order of photons in *Chandra*'s standard data reduction pipelines. Here, based on detector (ACIS) energy and position (dispersion distance or wavelength) of X-ray photons, it is possible to disentangle events into different spectral orders, as shown in so-called “banana” plots (Fig. B.1). Different event hyperbolas correspond to individual orders (left panel), but especially in observations of bright sources it can happen that not all events are assigned to their associated order, since the charge transfer efficiency in the detectors changes with source flux. This so called order-sorting problem is most prominent in the first order spectra (right panel). This problem can be solved by manually changing the default values in the Order Sorting and Integrated Probability (OSIP) file used by the `tg-resolve-events` routine of the standard data processing and ignoring the default values obtained from *Chandra*'s calibration database. Such a correction results in a much wider range of events entering the analysis (Fig. B.1).

Appendix C: Telemetry Saturation

A second problem occurring in sources with high flux is that because of the large count rates data are generated so fast that the telemetry stream may become saturated, causing an exposure gap in the corresponding time bin. The remaining data frame from the affected CCD chip is discarded (Fig. C.1c). Count rate light curves from observations affected by this problem – in our case ObsID 3815 – will erroneously show lower fluxes because they are commonly based on the average CCD exposure instead of treating countrates for each CCD separately. This problem can be dealt with by including exposure statistics from the secondary *Chandra* data in the *Chandra* standard processing using the tool `ag1c` (D. Huenemoerder, priv. comm.; see Fig. C.1).

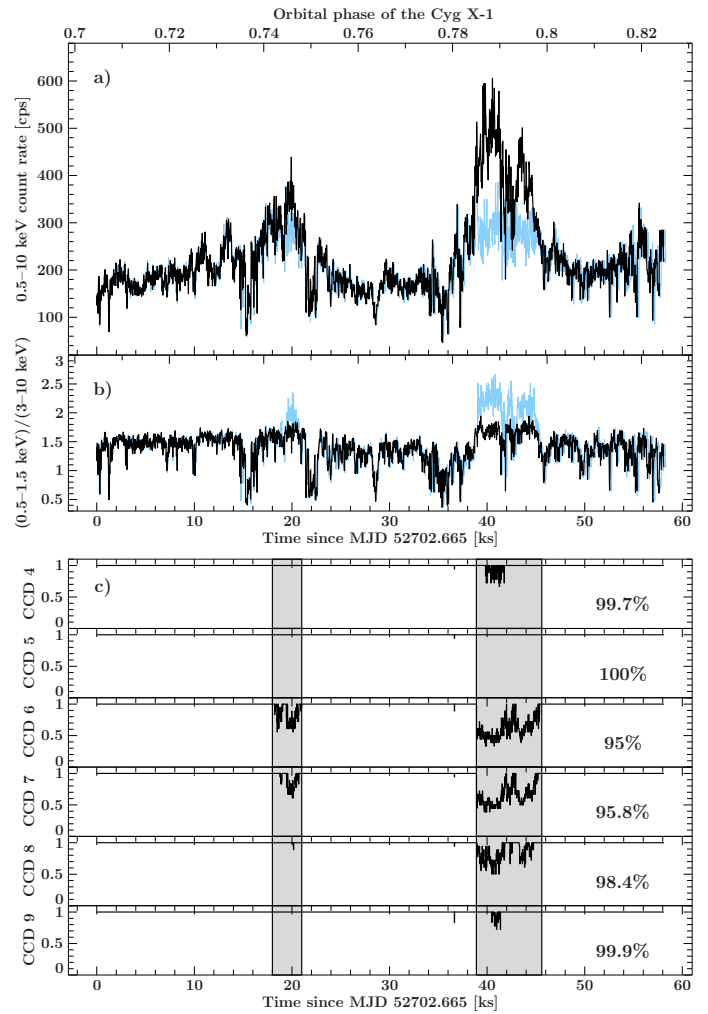


Fig. C.1. **a** 0.5–10 keV *Chandra* light curve of Cyg X-1 (time resolution of 25.5 s), obtained in 2003 March (ObsID 3815). Light blue: light curve without taking telemetry drop-outs into account. Black: light curve after correcting for telemetry drop-outs. **b** Ratio between the 0.5–1.5 keV and 3–10 keV energy bands, again with and without correction for the telemetry saturation. **c** Fractional exposure during the observation for each CCD. Telemetry drop-outs appeared at ~20 ks and after ~40 ks (gray regions). In the latter case, 5 of 6 CCDs were affected. Since whole data frames were discarded, lower countrates were observed in the light curve in the affected time intervals before the correction was applied (panel a). The spectrum extracted for those GTIs might be influenced as well, especially in the wavelength range of affected CCDs. These GTIs were not used in the analysis, even after correction of the count rates.

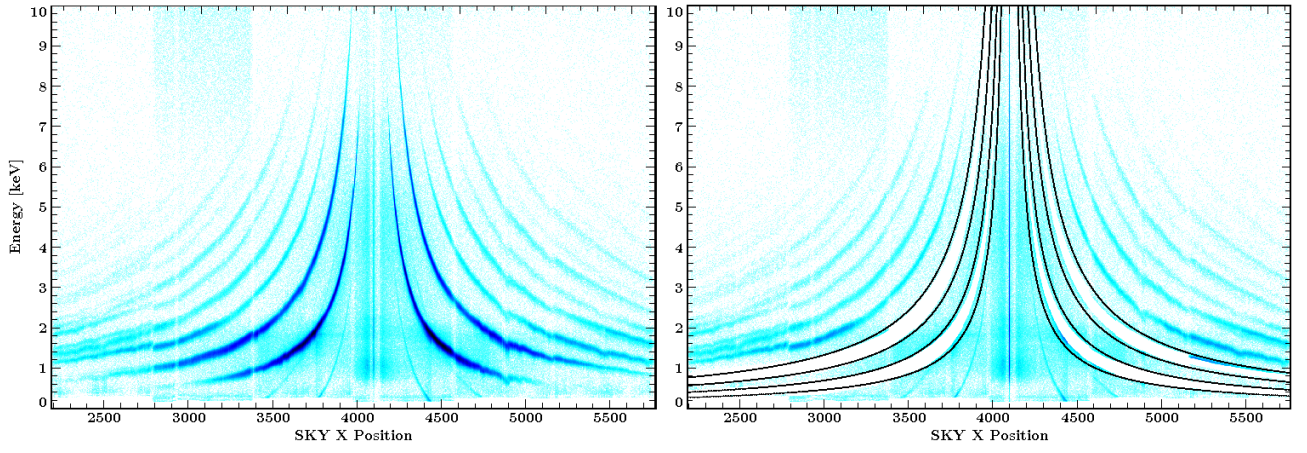


Fig. B.1. “Banana” plot – order-sorting of incoming events. **Left:** Diffraction orders for the HEG and MEG instruments. The source itself is located at sky x -position $x=4100$. The higher density of events around this region is most likely associated with a scattering halo. The different orders correspond to hyperbolas, shaped by a higher density of events. The hyperbolas with the highest event density, close to the source, represent the $\pm 1^{\text{st}}$ order of HEG and MEG. **Right:** Same as left figure, but showing the events assigned to the HEG and MEG in standard processing (white regions). Not all of the events are included. Changing the OSIP parameters as described in the text allows to include all events belonging to each order in the analysis (black lines).